DAAM mediates the assembly of long-lived, treadmilling stress fibers in collectively migrating epithelial cells in *Drosophila*

Kristin M Sherrard[1], Maureen Cetera[2,3], and Sally Horne-Badovinac[1,2,*]

Affiliations:

[1]Department of Molecular Genetics and Cell Biology, The University of Chicago.

[2]Committee on Development, Regeneration, and Stem Cell Biology, The University of Chicago.

[3]Current address: Department of Genetics, Cell Biology and Development, University of Minnesota.

*Correspondence to: shorne@uchicago.edu.

ABSTRACT

Stress fibers (SFs) are actomyosin bundles commonly found in individually migrating cells in culture. However, whether and how cells use SFs to migrate *in vivo* or collectively is largely unknown. Studying the collective migration of the follicular epithelial cells in *Drosophila*, we found that the SFs in these cells show a novel treadmilling behavior that allows them to persist as the cells migrate over multiple cell lengths. Treadmilling SFs grow at their fronts by adding new integrin-based adhesions and actomyosin segments over time. This causes the SFs to have many internal adhesions along their lengths, instead of adhesions only at the ends. The front-forming adhesions remain stationary relative to the substrate and typically disassemble as the cell rear approaches. By contrast, a different type of adhesion forms at the SF's terminus that slides with the cell's trailing edge as the actomyosin ahead of it shortens. We further show that SF treadmilling depends on cell movement and identify a developmental switch in the formins that mediate SF assembly, with DAAM acting during migratory stages and Diaphanous acting during post-migratory stages. We propose that treadmilling SFs keep each cell on a linear trajectory, thereby promoting the collective motility required for epithelial migration.

INTRODUCTION

Migrating cells rely on dynamic networks of filamentous actin (F-actin) for their motility. For cells migrating on two-dimensional substrates, these include the branched networks that underly lamellipodial protrusions (Ridley, 2011) and the stress fibers (SFs) that mediate much of the cell's interaction with the extracellular matrix (ECM). SFs are prominent F-actin bundles that have been categorized into different types based on their origin, subcellular location, and how they interact with non-muscle myosin II and integrin-based focal adhesions (Burridge and Guilluy, 2016; Burridge and Wittchen, 2013; Naumanen et al., 2008; Tojkander et al., 2012; Vallenius, 2013). The most studied SF types have myosin along their lengths and large focal adhesions at either end; these include ventral SFs (Hotulainen and Lappalainen, 2006; Tojkander et al., 2015) and the recently defined cortical SFs (Lehtimäki et al., 2021). SFs play key roles in focal adhesion maturation, defining the cell's front-rear axis, retraction of the trailing edge, and sensing the mechanical properties of the ECM (Lehtimäki et al., 2017; Livne and Geiger, 2016; Schwartz, 2010). However, our current knowledge of SFs in migrating cells comes almost entirely from studies of individual cells on non-native substrates. Whether and how cells use SFs to migrate *in vivo* or as part of a collective is largely unknown.

In this study, we use an *in vivo* system, the *Drosophila* egg chamber, to probe SF dynamics in collectively migrating epithelial cells (Cetera and Horne-Badovinac, 2015; Horne-Badovinac and Bilder, 2005). An egg chamber is an ovarian follicle that will give rise to one egg. It consists of a germ cell cluster surrounded by a somatic follicular epithelium (Figure 1A). During early stages of oogenesis, the follicle cells' basal surfaces crawl along the basement membrane ECM that that encapsulates the egg chamber (Cetera et al., 2014; Lewellyn et al., 2013). This causes the entire egg chamber to rotate within the basement membrane, which itself remains stationary (Haigo and Bilder, 2011). During this migration, each follicle cell has actin-based protrusions at its leading edge and a parallel array of SFs across its basal surface that are oriented in the direction of tissue movement (Cetera et al., 2014; Gutzeit, 1991) (Figure 1B). At later stages when the follicle cells have stopped migrating, the density of SFs across the basal surface increases (Delon and Brown, 2009; Gutzeit, 1991, 1990), and their contractile activity helps to create the elongated shape of the egg (Campos et al., 2020; He et al., 2010).

Here we show that the SFs in the follicle cells have many internal adhesions along their lengths, in addition to adhesions at the ends. We further show that these SFs undergo a novel treadmilling behavior that allows them to persist as the cell migrates over more than one cell length. Treadmilling SFs grow at their fronts by adding new adhesions and actomyosin segments over time. These front-forming adhesions remain stationary relative to the substrate, transition to being internal adhesions, and typically disassemble as the cell rear approaches. By contrast, a different type of adhesion forms at the SF terminus that appears to slide with the cell's trailing edge as the actomyosin segment ahead of it shortens. Blocking migration causes the internal adhesions to disappear and the treadmilling behavior to stop, which shows that the modular SF architecture depends on cell movement. We further identify a developmental switch in the formins required for SF assembly, with Disheveled-associated activator of morphogenesis (DAAM) contributing to treadmilling SFs during migratory stages and Diaphanous (Dia) contributing to the more canonical SFs that form once migration has ceased. We propose that treadmilling SFs ensure that each epithelial cell maintains a linear trajectory and thereby promote the highly orchestrated collective motility required for tissue-scale movement.

RESULTS

Migrating follicle cells have long-lived, treadmilling SFs

To visualize SF dynamics in living follicle cells, we used GFP-tagged and mCherry (mCh)-tagged versions of the regulatory light chain of myosin II (MRLC, Spaghetti Squash in *Drosophila*) (Figure 2A) and near total internal fluorescence (near-TIRF) microscopy (Movie S1). Live actin labels are less effective markers because they strongly label leading-edge protrusions, which obscures the SF tips; they can also disrupt F-actin organization (Figure S1A-D). This imaging strategy allowed us to watch SFs appear and disappear over time as the follicle cells migrated. Appearance of a new SF is marked by a rapid coalescence of MRLC (Figure 2B). SFs disappear either by fading along their lengths or by contracting rapidly from the rear (Figure 2C).

We measured SF lifetimes by identifying individual SFs at the mid-point of a 60-minute movie and tracking their behavior over the full imaging period (Figure 2D). Only actomyosin fibers that spanned at least half the cell's length were tracked. Through this assay, we determined that these SFs have a half-life of 34 minutes. This is clearly an underestimate, however, as only 60% of SFs both appeared and disappeared during the 60 minute window. For 32% of SFs, we saw either their appearance or disappearance but not both. The remaining 8% persisted for the entire 60 minutes. We then used the same dataset to analyze the relationship between SF lifetimes and the distance travelled by the cell. The follicle cells migrated a mean distance of 16.8 µm in this assay, corresponding to a mean of 2.2 cell lengths. Strikingly, 62% of SFs persisted for longer than the time required for the cell to travel at least one cell length (Figure 2E). Given that SFs are attached to an immobile substrate by integrin-based adhesions, we reasoned that the entire actomyosin fiber must be treadmilling (i.e., growing at the front and shrinking at the back). Indeed, new actomyosin segments are added to the front of existing SFs (Figures 2F-2H, S1E-S1F, and Movie S2), which explains their persistence. Hereafter we refer to these long-lived SFs as “treadmilling SFs”.

Treadmilling SFs have many adhesions along their lengths

To understand the treadmilling behavior of the SFs, we examined their associated integrin-based adhesions. Previous descriptions of these adhesions in follicle cells primarily focused on later stages of egg chamber development (Delon and Brown, 2009), after the follicle cells have ceased migrating. At these later stages, the SFs are increased in density across the basal surface, and they exhibit the canonical organization with large focal adhesions at their ends (Figure 3A and 3H). By contrast, the SFs present during migratory stages have many smaller adhesions along their lengths (Figures 3B-3H, S2) (Cetera et al., 2014), with an average of 5.5 adhesions per SF. This phenomenon is easiest to see when Paxillin-GFP is overexpressed (UAS-Pax-GFP); however, we also see multiple adhesions with endogenous GFP tags on Paxillin, Talin, and the ßPS-integrin subunit, Myospheroid. Thus, the SFs in migrating follicle cells have internal adhesions, in addition to adhesions at their ends.

Adhesions are added to the front and removed near the back of treadmilling SFs

To determine how the internal adhesions relate to the treadmilling behavior we saw with MRLC, we imaged epithelia in which MRLC was expressed in all cells and UAS-Pax-GFP was expressed in a subset of cells (Figures 4A-4D and Movie S3). This allowed us to identify an individual SF using the MRLC signal and then watch the adhesions appear and disappear with the Paxillin signal. Kymographs of individual SFs showed that new adhesions are continuously added to the front of a SF over time (Figure 4A). A front-forming adhesion typically first appears near the cell’s leading edge and grows in brightness as an actomyosin segment coalesces behind it to link the new adhesion to an existing SF (Figure 4C). New adhesions are also pulled slightly rearward, consistent with their maturing under tension. The front-forming adhesions then remain stationary relative to the basement membrane substrate.

We noted that a different type of adhesion forms at the back of the cell. For 82% of the SFs analyzed, the final adhesion at the SF terminus appears to slide along the substrate at the same speed that the cell migrates (Figures 4A and 4D). Sliding adhesions can arise from stationary adhesions; however, 80% arise *de novo* near the cell's trailing edge. Sliding adhesions are remarkably long-lived, persisting for a mean of 34 minutes, which corresponds to the time required for a cell to migrate 1.2 cell lengths. By contrast, stationary adhesions persist for only a mean of 13 minutes (Figure 4E). Stationary adhesions typically disassemble before they reach the cell's trailing edge. However, ~20% of stationary adhesions are subsumed by sliding adhesions (Figure 4D and Movie S4). We observed that 74% of sliding adhesions merged with at least one stationary adhesion, which may account for their long lifetimes.

In summary, a treadmilling SF grows at its front by incorporating new adhesions and new actomyosin segments over time. These front-forming adhesions remain stationary relative to the substrate and typically disassemble as the cell rear approaches. By contrast, a sliding adhesion forms at the SF terminus that appears to move with the cell's trailing edge as the actomyosin segment in front of it shortens (Figure 4F).

The modular architecture and treadmilling behavior of the SFs depends on cell migration

Because new adhesions are added to the front of a treadmilling SF as the cell's leading-edge advances, it seemed likely that the treadmilling behavior would depend on cell movement. We blocked follicle cell migration by employing two methods that eliminate leading-edge F-actin networks in these cells, inhibition of Arp2/3 by CK-666, and depletion of the Scar/WAVE complex with RNAi against Abelson interacting protein (*Abi RNAi*). Analysis of fixed samples revealed that both treatments cause SFs to adopt a canonical SF architecture, in which the adhesions become concentrated at the ends (Figure 5A).

We then used live imaging to explore how this structural transition occurs. Following addition of CK-666, the follicle cells gradually come to a stop. The internal adhesions disappear over time as the end adhesions grow and myosin becomes concentrated in the center (Figure 5B and Movie S5). Once this transition is complete, individual SFs often contract from both ends toward the center and disappear; new adhesions are never added to their ends (Figure 5C).

The transition from a modular to a canonical SF architecture could be due to loss of cell migration; however, it could also be due to loss of some other activity that depends on the

Scar/WAVE complex. To distinguish between these possibilities, we examined SFs in clones of cells expressing RNAi against the Abi or Sra1 components of the Scar/WAVE complex. These mosaic epithelia retain the ability to migrate because the RNAi-expressing cells are carried along by their wild-type neighbors (Cetera et al., 2014). Importantly, the SFs within the RNAi-expressing clones show the same modular architecture and treadmilling behavior as wild-type SFs (Figures 5D and 5E). We therefore conclude that it is migration itself, not the activity of the Scar/WAVE complex, that is necessary to generate treadmilling SFs.

DAAM mediates the assembly of treadmilling SFs

To better understand how treadmilling SFs are built, we sought to identify the source of their F-actin. We first considered that branched F-actin networks flowing back from leading edge lamellipodia could be incorporated into the SFs. However, elimination of leading-edge F-actin networks through depletion of the Scar/WAVE complex did not reduce F-actin levels in the SFs (Figures 6A, 6D, S3A and S3C). This is also true for cells depleted of Enabled, which builds leading-edge filopodia (Figures S3B and S3C) (Cetera et al., 2014). Hence, the leading edge is not a major source of F-actin for the SFs.

We next asked if formins are required, as these proteins assemble unbranched F-actin and are often associated with SF formation (Kühn and Geyer, 2014; Valencia and Quinlan, 2021). We performed an RNAi-based screen of *Drosophila* formins and found that depleting DAAM reduces F-actin levels in the SFs by ~30% (Figures S3D, 6B and 6D). We confirmed this result by showing that two null alleles of *DAAM* similarly reduce F-actin in the SFs without having obvious effects on other F-actin populations (Figure 6B, 6D and 6E). An activated form of DAAM increases F-actin in the SFs, but this effect is not statistically significant (Figure 6C). RNAi against other formins had no effect on the SFs, nor did co-depleting formins or other F-actin assembly factors with DAAM (Figures S3D and S3E). It is important to note, however, that we do not know that all the formin RNAi transgenes we screened are functional. From these data, we conclude that DAAM is a key contributor to treadmilling SF assembly.

Finally, we asked how DAAM contributes to treadmilling SFs. Using a line in which DAAM is endogenously tagged with GFP (DAAM-GFP) (Molnár et al., 2014), we found that DAAM localizes largely uniformly within the cortex with no obvious enrichment on SFs or adhesions (Figure 7A and 7B). DAAM-depleted cells have the same density of SFs across their basal surfaces as control cells (Figure 7C, 7D); each SF simply has reduced levels of F-actin, myosin, and the focal adhesion protein Talin (Figures 7E, 7F). These findings suggest that DAAM-depleted cells may adhere less well to the ECM. We previously showed that a mild reduction in cell-ECM adhesion increases the speed of follicle cell migration (Lewellyn et al., 2013). Similarly, mean migration rates for DAAM-depleted epithelia are faster than for control epithelia (Figure 7G). Altogether, these data suggest that DAAM contributes to the assembly and/or maintenance of treadmilling SFs by adding new F-actin along their lengths, and/or by contributing F-actin to the basal cortex, and that this additional F-actin strengthens cell-ECM adhesion.

There is a developmental switch in the formins that build treadmilling vs. canonical SFs

One striking feature of the SFs in the follicle cells is that they change in both structure and function between early developmental stages when they mediate collective cell migration and later stages when their contractility helps to create the elongated shape of the egg, so we next investigated the molecular mechanisms that underly this transition. We found that DAAM is downregulated after follicle cell migration has ceased (Figure 8A). This observation suggested that DAAM might mediate the formation of treadmilling SFs in migratory cells but not the more canonical SFs that form at later stages. To test this idea, we used traffic jam-Gal4 to express *DAAM RNAi* in the follicle cells throughout oogenesis. This reduces F-actin in the treadmilling SFs as expected. During post-migratory stages, however, F-actin levels in the SFs are unaffected (Figure 8B). Thus, DAAM selectively contributes to the formation of treadmilling SFs.

Previous work suggested that the formin Diaphanous (Dia) is required for SF assembly in the follicle cells (Delon and Brown, 2009; Popkova et al., 2020). However, when we depleted Dia during migratory stages as part of our RNAi screen, the treadmilling SFs were unaffected (Figures 8C and S3D). We know Dia was depleted because the RNAi-expressing clones contained multi-nucleated cells, consistent with Dia's role in cytokinesis. To ask if Dia selectively mediates canonical SF assembly during post-migratory stages, we expressed *Dia RNAi* using Cy2-Gal4, which initiates expression after cell divisions and cell migration have both ceased. This condition largely eliminates SFs from post-migratory cells, while similarly expressing *DAAM RNAi* does not (Figures 8D and 8E). These data show that there is a developmental switch in the formins that mediate SF assembly in the follicle cells, with DAAM contributing to treadmilling SFs during migratory stages and Dia contributing to the canonical SFs that form after migration is complete.

DISCUSSION

SFs are a common and well-studied feature of cells migrating on non-native substrates *in vitro*. However, whether and how cells use SFs to migrate on their native substrates *in vivo* remains largely unexplored. Focusing on the follicular epithelial cells of *Drosophila*, we found that their SFs display a novel treadmilling behavior that allows individual SFs to persist as the cells migrate over more than one cell length. The discovery of these long-lived contractile structures has important implications for our understanding of SF dynamics, the influence that different SF types can have on cell motility, and how SF structure and function can change as a tissue develops, each of which is discussed below.

We found that SFs in migrating follicle cells have internal adhesions along their lengths, in addition to adhesions at the ends. These internal adhesions are key to the treadmilling behavior. When a new adhesion and actomyosin segment are added to the front of an existing SF, the previous front adhesion becomes an internal adhesion. In this way, the formation of internal adhesions depends on treadmilling. Once formed, the internal adhesions then contribute to treadmilling by generating the modular SF architecture needed for older stationary adhesions to be disassembled near the cell's rear and allow the back of the SF to shorten. To our knowledge this is the first study to focus on the role of internal adhesions in SF dynamics, but there are hints in the literature that these structures may exist in other cells. For example, SFs isolated from human foreskin fibroblasts and bovine endothelial cells have small puncta of the focal adhesion protein vinculin along their lengths in addition to prominent vinculin puncta at their ends (Katoh et al., 1998), and the cortical SFs in cultured mesenchymal cells were sometimes observed to have more than two adhesions (Lehtimäki et al., 2021). Internal adhesions have also been invoked as a possible explanation for the buckling pattern observed when SFs are rapidly compressed (Costa et al., 2002; Kassianidou and Kumar, 2015). Because internal adhesions are attached to two aligned actomyosin segments, they likely experience more balanced pulling forces than end adhesions, which may affect their composition and/or organization. It is also likely, however, that there is still higher tension on one side of the adhesion due to forces exerted by cell movement. Determining the extent to which internal adhesions are found in other cell types and how they differ from end adhesions represent important areas for future research.

A treadmilling SF grows at its front when a new adhesion and new actomyosin segment appear nearly simultaneously ahead of the foremost adhesion. How do these new elements arise? We envision that the new actomyosin segment captures a nearby nascent adhesion that has formed just behind the cell's leading edge, and that this activity both links the nascent adhesion to the existing SF and induces it to mature. Our finding that DAAM is required for robust SF formation also suggests two hypotheses for the source of the F-actin for the new actomyosin segment. One possibility is that DAAM localizes to nascent and mature adhesions, causing actin filaments to grow out from these sites, like the role ascribed to Dia in dorsal SF formation (Hotulainen and Lappalainen, 2006; Oakes et al., 2012; Tojkander et al., 2011). Bundling of the DAAM-generated filaments by myosin could then link the nascent adhesion to the mature adhesion. Alternatively, DAAM could play a more general role in contributing F-actin to the basal cortex (Chugh and Paluch, 2018), with local pulses of myosin activity near the cell's leading-edge condensing the cortical F-actin meshwork to form the new actomyosin segment. We favor the second model for two reasons. First, DAAM is found throughout the cortex with no obvious enrichment at adhesions. Second, treadmilling SFs closely resemble other SF types that arise from the cortex and/or are embedded within it (Lehtimäki et al., 2021; Svitkina, 2020; Vignaud et al., 2020), as they lie so flat against the basal surface that we can visualize them with near-TIRF microscopy. This contrasts with ventral SFs whose center can arch away from the migratory surface. However, future work will be required to distinguish between these possibilities.

A treadmilling SF shrinks at its back using a mechanism involving an adhesion that slides along the substrate as the actomyosin segment in front of it shortens. These rear-most sliding adhesions are strikingly similar to those found in individual migrating cells in culture (Ballestrem et al., 2001; Digman et al., 2008; Laukaitis et al., 2001; Rid et al., 2005; Smilenov et al., 1999; Wehrle-Haller and Imhof, 2003), in that they primarily form near the cell's trailing edge and then track with its movement. In migrating cells, sliding adhesions have been proposed to act as rudders that help to steer the cell (Rid et al., 2005). In stationary cells, sliding adhesions can also remodel the ECM (Lu et al., 2020; Zamir et al., 2000). Given that one of the purposes of follicle cell migration is to polarize the basement membrane ECM over which they move (Gutzeit, 1991; Haigo and Bilder, 2011; Isabella and Horne-Badovinac, 2016), it is interesting to speculate that sliding adhesions could function in both roles in these cells.

The modular architecture and unidirectional growth of a treadmilling SF both depend on cell movement. We found this relationship by comparing two conditions that eliminate leading-edge protrusions. In one condition, we eliminated protrusions from a clone of cells. Here, the epithelium continues to migrate, carrying the non-protrusive cells along for the ride (Cetera et al., 2014). The SFs in the clone are indistinguishable from those in wild-type cells, showing that protrusive F-actin networks are not required for treadmilling SFs to form. In the other condition, we eliminated protrusions from the entire tissue, which does block epithelial migration. Here, the SFs transition to having large adhesions only at their ends, but they are not stationary. Instead, when a new SF forms, it continuously shortens toward the middle until it disappears with no new material added to the ends. This movement is reminiscent of the way a treadmilling SF normally shortens at its rear, except that it happens from both ends. This raises the possibility that these SFs have lost their polarity and have two “backs”. If true, studies of these aberrant SF dynamics could help to reveal how a treadmilling SF becomes polarized for unidirectional movement.

We propose that treadmilling SFs may be particularly well suited to mediate the collective migration of epithelial cells. Cells that migrate as individuals can undergo frequent turns as they explore their environment. By contrast, each follicle cell follows a roughly linear trajectory over its entire migratory period, which can last for up to two days of egg chamber development (Cetera et al., 2014; Horne-Badovinac and Bilder, 2005). The follicle cells use intercellular signaling to align all their front-rear axes in the same direction across the tissue (Barlan et al., 2017; Stedden et al., 2019). Once this alignment is achieved, however, the long lifetimes and unidirectional growth of their SFs likely reinforce this tissue-scale order by ensuring that each cell maintains the linear trajectory required for the entire epithelium to move in a directed way. Given that the collective migration of epithelial cells plays central roles in morphogenesis, turnover of the intestinal lining, wound repair, and the metastatic cascade (Friedl and Gilmour, 2009; Jain et al., 2021; Mishra et al., 2019; Scarpa and Mayor, 2016), the use of treadmilling SFs to direct cell motility in natural contexts may be widespread.

Finally, this work highlights how SFs within a given cell type can change in both their structure and mode of assembly as a tissue develops. When follicle cell migration ends, the SFs take on a new morphogenetic role in which their contractile activity helps to create the elongated shape of the egg (Campos et al., 2020; He et al., 2010). This change in function is accompanied by a change in SF organization, in which the density of SFs across the basal surface increases, internal adhesions disappear, and large focal adhesions become concentrated at the SFs’ ends. Previous work revealed that the focal adhesions associated with the two SF types differ, with αPS1/ßPS being present during migratory stages and αPS2/ßPS taking over after migration is complete; Tensin is also only present in post-migratory stages (Delon and Brown, 2009). We have now found that even the mode of F-actin assembly differs, with DAAM mediating the formation of migratory SFs and Dia mediating their formation post-migration, a result that is consistent with previous studies of Dia in the follicle cells (Delon and Brown, 2009; Popkova et al., 2020). Why a different formin provides the F-actin for each type of SF is not immediately clear. However, this observation further underscores the importance of studying SFs in developing tissues where such structural transitions can and do occur.

Altogether, this work defines a new type of long-lived, treadmilling SF that appears to be ideally suited for collectively migrating epithelial cells *in vivo*. It further highlights how studying SFs in a natural context can reveal unexpected changes in the mechanisms that underly their assembly as a tissue develops.

MATERIALS AND METHODS

***Drosophila* genetics**

We cultured *D. melanogaster* on cornmeal molasses agar food using standard techniques and performed all experiments on adult females. For most experiments, we raised crosses at 25ºC and aged experimental females on yeast with males for 2-3 days at the same temperature. For tissue-wide depletion of Abi, which causes round eggs that block the ovary, we dissected females no more than 2 days after eclosion. Experimental genotypes for each figure panel are in Table S1.

We produced clones of either *DAAM*^{A} or *DAAM*^{Ex68} mutant cells or DAAM-GFP expressing cells using FRT19A with the heat shock promoter driving FLP recombinase expression. For Flp-out clones, we crossed UAS lines to flies with FLP recombinase under a heat shock promoter and an Act5c>>Gal4 Flp-out cassette with or without UAS-RFP. We induced heat shock by incubating pupae and adults at 37ºC for 1 hour, followed by 1 hour of recovery at 25ºC, and then another hour at 37ºC. We performed this heat shock procedure approximately 6 times over the course of 3-4 days.

Stocks are from the Bloomington Drosophila Stock Center or the Vienna Drosophila Resource Center (see Table 1 for details) with the following exceptions: traffic jam-Gal4 (104-055), UAS-*Abi RNAi* (NIG9749R-3) and Pax-GFP (109-971) are from the Drosophila Genetic Resource Center in Kyoto; *DAAM*^{Ex68}, UAS-Utr-ABD-GFP is a gift of Thomas Lecuit (Rauzi et al., 2010), UAS-C-DAAM (Matusek et al., 2006), DAAM^{Ex68} (Dollar et al., 2016), and DAAM-GFP (Molnár et al., 2014) are gifts from József Mihály; UAS-Moe-ABD-mCh is a gift of Brooke McCartney, UAS-

Pax-GFP is a gift of Denise Montell (He et al., 2010); MRLC-mCh is a gift of Eric Wieschaus (Martin et al., 2009); β-Integrin/Mys-GFP is a gift from Nick Brown (Klapholz et al., 2015); Talin-GFP is gift from Hugo Bellen (Venken et al., 2011); Cy2-Gal4 is a gift from Nir Yakoby (Queenan et al., 1997).

Time lapse video acquisition and microscopy

We performed live imaging of egg chambers largely as described (Cetera et al., 2016), with the exact procedure outlined below. We collected experimental females 0-2 days after eclosion and aged them on yeast for 1-2 days. We dissected ovaries in live imaging media (Schneider’s Drosophila medium containing 15% fetal bovine serum (FBS) and 200 mg/mL recombinant human insulin (Sigma)), also in some experiments containing CellMask Green (Thermo-Fisher; 1:500), or Orange or Deep Red Plasma MembraneStain (Thermo-Fisher; 1:1000). After carefully removing the muscle sheaths with forceps, we transferred individual ovarioles to fresh live imaging media to wash out excess CellMask, then transferred ovarioles and media to a glass slide, adding 51 µm Soda Lime Glass beads (Cospheric LLC) to support a 22 x 30 mm No. 1.5 coverslip. We sealed the edges of the coverslip with Vaseline to prevent evaporation. Each slide was used for no more than 1.5 hours. We examined all egg chambers for damage prior to imaging.

We imaged egg chambers using a Nikon ECLIPSE-Ti inverted microscope equipped with a Ti-ND6-PFS Perfect Focus Unit. A laser merge module (Spectral Applied Research) controlled 481-nm and 561-nm laser excitation from 50 mW solid-state lasers (Coherent Technology) to a motorized TIRF illuminator. We adjusted the laser illumination angle to achieve near-TIRF illumination (Tokunaga et al., 2008). We collected images using a Nikon CFI 100x Apo 1.45 NA oil immersion TIRF objective combined with 1.5x intermediate magnification onto an Andor iXon3 897 EMCCD camera. All image acquisition was controlled using MetaMorph software. We obtained time-lapse movies by capturing single planes near the basal epithelial surface every 10-30 sec.

We used ImageJ (Schindelin et al., 2012; Schneider et al., 2012) to set minimum and maximum pixel values and in Figure 1A to perform gamma adjustment on the original 16-bit image data, before converting images to 8-bit grayscale format for display. We performed these operations identically for all images that are compared directly.

Analyses from Live Imaging Data

To calculate epithelial migration rates, we generated kymographs from the time-lapse image stacks in ImageJ (Schindelin et al., 2012; Schneider et al., 2012) by drawing a single line across several cell diameters in the direction of migration. We determined the migration rate for each epithelium by measuring the slope of 3-4 kymograph lines and averaging the values. Please see (Barlan et al., 2017) for an illustration of this technique.

To measure lifetime of individual SFs, we began at the midpoint of hour-long movies (imaged at 10 sec or 20 sec intervals) of egg chambers expressing MRLC-mCh or -GFP. We selected one SF at a time from cells that remained in view for the entire movie, and ran the movie backwards to identify its frame of origin (if any) and forwards to identify its frame of disappearance (if any). Because egg chambers kept on slides for longer than an hour often exhibited a slowing of migration, we did not attempt to measure SF lifetime from longer movies. We expressed SF lifetime both in minutes and in cell lengths by calculating each egg chamber’s migration speed as described above, and by measuring front-rear cell length at the cell’s middle at the movie’s midpoint.

To measure lifetime and behavior of individual adhesions, we imaged egg chambers expressing MRLC-mCh and Pax-GFP under the patchy driver da-Gal4 (to allow delineation of individual cells) for one hour at 10 or 20 sec intervals. As described for SFs above, we identified adhesions in the midpoint of these movies and followed them frame-by-frame, backwards and forwards, to find their time of origin and disappearance. Two mostly distinct populations of adhesions were found, one that remained in place after forming near the front or in the middle of cells (“stationary adhesions”) and one that slid at the same rate as the migrating cells, invariably found near the rear (“sliding adhesions”). Their lifetime data was tabulated separately. Sliding adhesions frequently exhibited merging behavior with stationary adhesions, and this, as well as the proportion of SFs that had a sliding adhesion at a given time, was noted.

To produce the kymographs shown in Figure 4, we aligned images so that the anterior–posterior axis of the egg chamber coincided with the horizontal (x) image axis. For Figure 4A, we selected rectangular regions aligned with the x image axis, whose width (in x) coincided with the width of a single SF and whose height (in y) corresponded to the front-rear length of the cell. From the original image stack, we extracted an xyt substack corresponding to this rectangular region. We then applied ImageJ’s Reslice tool to this stack with respect to the x-t plane, then used a maximum-intensity projection to collapse the individual slices in y to obtain a kymograph in x vs. t. For the kymograph shown in Figure 4C, we similarly selected a rectangle the width of a single

SF but only 25 pixels high, corresponding to the front end of the SF, and performed a summed projection rather than a maximal projection, in order to describe the total change in brightness across the width of the SF.

For CK-666 treatments, we dissected egg chambers expressing MRLC-mCh and endogenous Pax-GFP as described above, then separated out older ones leaving only stage 9 and younger egg chambers. We placed egg chambers into a final concentration of 1.5 mM CK-666 or the equivalent concentration of DMSO for controls, and either made the slide immediately or after incubating for a period, commencing imaging within a range of 6-70 minutes.

Fixed image acquisition and microscopy

We dissected ovaries in live imaging media, as described above, removing muscle sheaths with forceps during dissection to isolate individual ovarioles. We fixed egg chambers for 15 minutes in 4% EM grade formaldehyde (Polysciences) in PBT (Phosphate buffered saline + 0.1% Triton X-100), and washed them 3x in PBT. To stain with phalloidin, we incubated them in TRITC or AlexaFluor-488 phalloidin (both 1:200, Sigma), or AlexaFluor-647 phalloidin (1:100), for 30 minutes at room temperature or overnight at 4ºC, then washed 3x in PBT and mounted them with one drop of SlowFade Antifade (Invitrogen) or Slowfade Diamond Antifade (Invitrogen) onto a slide with a 22 x 50mm No. 1.5 coverslip. For antibody staining (DAAM-GFP only), we fixed and washed egg chambers as above, and incubated them at 4ºC overnight with an anti-GFP-Alexa488 antibody. (1:200, Invitrogen), washed them 3x over 30 minutes, and mounted them as above.

We imaged tissue using one of two laser-scanning confocal microscopes, either a Zeiss LSM 800 with a 40x/1.3 NA EC Plan-NEOFLUAR objective or a 63x/1.4 NA Plan-APOCHROMAT objective running Zen 2.3 Blue acquisition software, or a Zeiss LSM 880 with 40x/1.3 Plan-APOCHROMAT or 63x/1.4 NA Plan-APOCHROMAT objective and a Zeiss Airyscan running Zen 2.3 Black acquisition software to improve resolution and signal-to-noise ratio. For all images a single confocal slice is shown. We did all image processing using ImageJ, as described in the video microscopy section.

For CK-666 treatments, we dissected egg chambers expressing MRLC-mCh and endogenous Pax-GFP as described above, then separated out older ones leaving only stage 9 and younger egg chambers. We transferred them to 500 µL live imaging medium containing either 1.5 mM CK-666 in DMSO or the same concentration of DMSO alone and incubated covered for one hour at 25ºC before fixing both as described above.

Measurements from Fixed Imaging Data

We measured the spacing and number of adhesions on SFs from confocal images of endogenously tagged Pax-GFP (DGRC 109-971) co-stained with AlexaFluor-647 phalloidin. We selected individual SFs (all those within a given cell that spanned at least half the cell length, and well separated from nearby SFs) using a segmented line, 4 pixels wide, in the phalloidin channel. We measured the length of this line, then used the Straighten function and the Find Peaks macro in ImageJ (using the default settings of minimum amplitude 44.8 and minimum distance 0) to count number of bright, separate paxillin spots.

We measured SF lateral spacing from images taken in Airyscan mode of stage 7 egg chambers stained with phalloidin, containing control and *DAAM*^{A} mutant mitotic clones. We began by taking a line scan across the middle of the cell just inside the lateral membrane with ImageJ' s Plot Profile tool, and identified individual SFs as having a gray value over 500 (16-bit data) and being at least 0.5 µm from adjoining peaks. Line scans taken at the front and rear of the cells yielded very similar lateral spacings, indicating this does not vary across the length of the cell. We calculated lateral spacing as the number of SFs occurring across the width of the line scan.

To quantify mean brightness of basal structures in ImageJ, we used single confocal sections of the basal epithelial surface. For relative SF brightness, we used egg chambers mosaic for a DAAM loss of function mutation or Flp-out clones driving RNAi. We employed the irregular polygon tool to manually outline cells, excluding the lateral membrane and leading-edge structures, and measured mean fluorescence intensity of 10 experimental cells and 10 nearby control cells in each egg chamber, and calculated a ratio for each egg chamber. We selected cells in close proximity to avoid possible effects from anterior-posterior gradients along the egg chamber. We employed the same technique to quantify Talin-GFP brightness in egg chambers clonally expressing DAAM RNAi or overexpressing activated C-DAAM.

To quantify MRLC brightness, we compared egg chambers expressing *DAAM RNAi* in the entire follicular epithelium to control egg chambers, measuring the majority of the field of cells in view on the slide, but excluding regions near the edge of the egg chamber. We similarly quantified levels of DAAM-GFP (in egg chambers stained with antibody to GFP).

Quantification and Statistical Analysis

All data were obtained from at least two independent experiments, and several females were analyzed each time. All data were highly reproducible. No statistical method was used to predetermine sample size. The sample size for each experiment can be found in the figure legend. We tested data for normality using the D'Agnostino & Pearson test for sample sizes above 8, and the Shapiro-Wilk test for sample sizes below 8. In nearly all cases data were normally distributed, but we chose to use non-parametric statistics as more appropriate for the low and uneven sample numbers. We used two-tailed, Wilcoxon matched-pairs signed ranks tests, or Mann-Whitney tests, to determine if two datasets were significantly different, with Dunnett's correction when comparing multiple datasets.

Notably, non-parametric statistical tests are less powerful than the corresponding parametric versions, and thus provide a more stringent test of significance. Therefore, we also performed 2-tailed ratio paired t-tests (Figures 6D, S3C, S3D, 7F, 8B) and unpaired 2-tailed t-tests (Figure 8D) or ANOVA followed by Dunnett's correction for multiple comparisons (Figure S3E), to ensure that we were not failing to reject the null hypothesis of no effect from genetic manipulations. Only in the case of C-DAAM did the parametric test detect significance not seen by the corresponding non-parametric one: both SF brightness (Figure 6D) and Talin levels (Figure 7F) had p-values < 0.05 in paired t-tests.

Analysis was performed using Prism software, version 8 (GraphPad). Experiments were not randomized, nor was the data analysis performed blind. Egg chambers damaged by the dissection process were not included in the analysis.

ACKNOWLEDGEMENTS

We thank Hugo Bellen, Nick Brown, Thomas Lecuit, József Mihály, Brooke McCartney, Denise Montell, Eric Wieschaus, and Nir Yakoby for generously sharing reagents. We are also grateful to Yvonne Beckham, Lindsay Llewellyn and members of the Horne-Badovinac lab for comments on the manuscript. This work was funded by a grant from the Seaver Institute to Kristin Sherrard, NIH T32 GM007183 to Maureen Cetera, and NIH R01 GM126047 to Sally Horne-Badovinac.

COMPETING INTERESTS

The authors declare no competing interests.

AUTHOR CONTRIBUTIONS

Kristin Sherrard, Conceptualization, Formal analysis, Validation, Investigation, Visualization, Methodology, Writing - original draft, Writing - review and editing; Maureen Cetera, Conceptualization, Methodology, Writing - review and editing; Sally Horne-Badovinac, Conceptualization, Supervision, Funding acquisition, Project administration, Writing - original draft, Writing - review and editing.

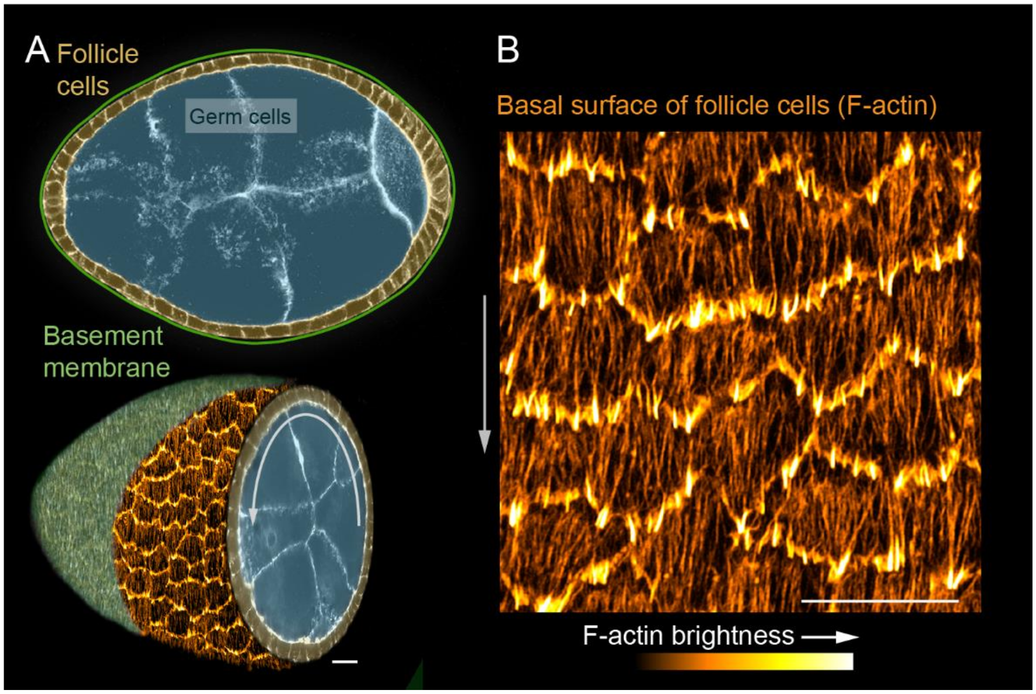

Figure 1. Introduction to the SFs in collectively migrating follicle cells

(A) Composite images of an egg chamber (pseudocolored), transverse section above and 3D cutaway view below. Curved arrow shows the rotational migration of the follicle cells as they crawl along the basement membrane ECM (drawn as a line in upper image, from a confocal section of Collagen-IV-GFP in lower image).

(B) Image of the basal surface of the follicular epithelium. Each cell has a leading-edge protrusion (yellow) and a parallel array of SFs (orange) oriented in the direction of migration.

Experiments performed at stage 7. Grey arrows show migration direction. Scale bars 10 µm.

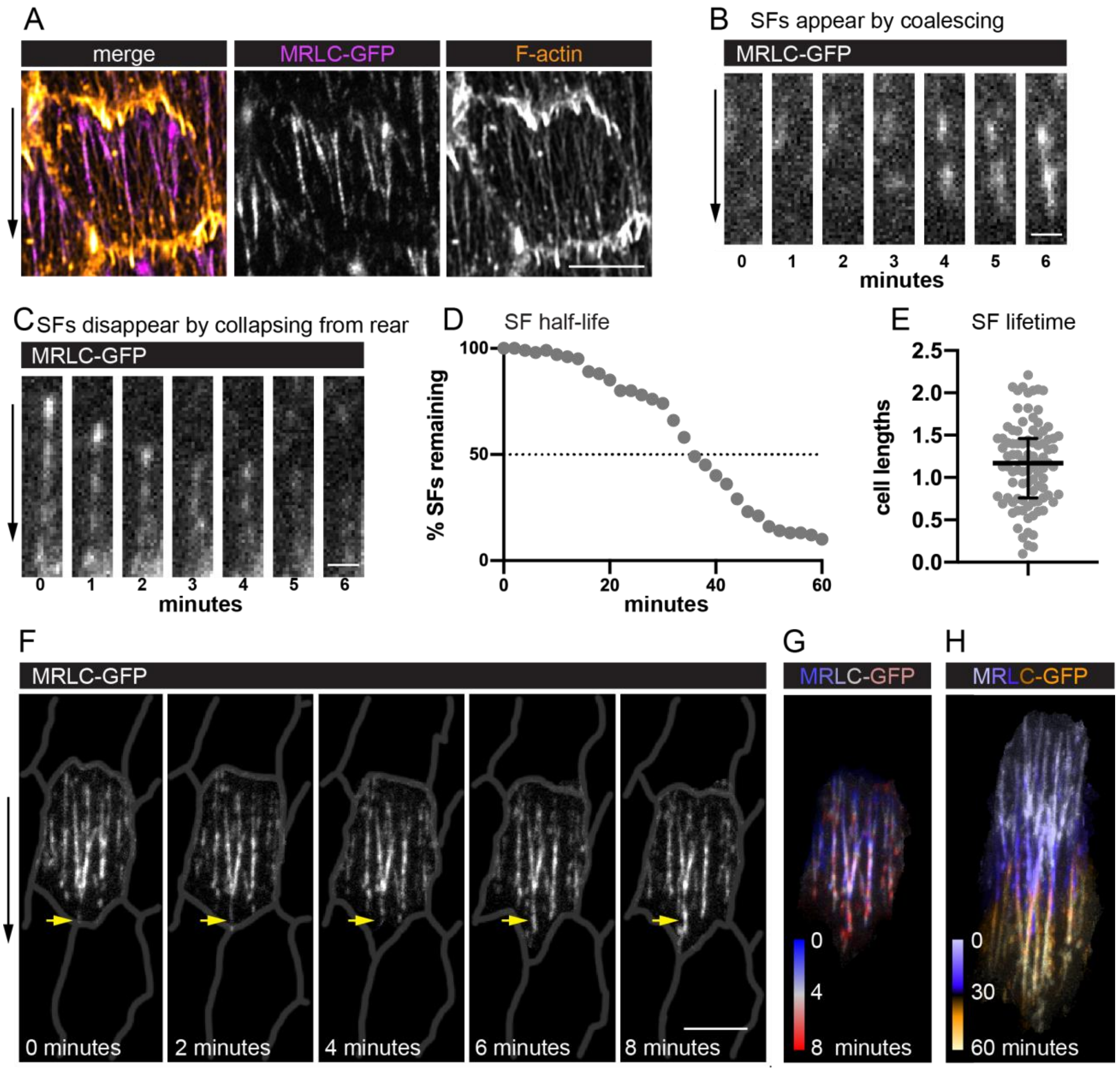

Figure 2. Migrating follicle cells have long-lived, treadmilling SFs

(A) Image of one cell showing that myosin regulatory light chain (MRLC-GFP) labels SFs, but not leading-edge protrusions.

(B, C) Still images from movies showing a SF (B) forming by MRLC-GFP coalescence, and (C) disappearing by collapsing from the rear.

(D, E) Quantification of SF lifetimes. (D) Half-life measurement in real time. (E) Lifetimes as a function of how long it took the cell to migrate one cell length. n=91 SFs from 23 cells in 3 egg chambers. Bars in (E) show median and interquartile ranges.

(F) Still images from a movie of an optically isolated cell showing a SF tip growing as the cell migrates (arrow). Cell outlines are drawn from membrane label. See Movies S1 and S2.

(G, H) Temporal projections of SFs from the cell in (F). (G) Shows the same period as (F) at 20-second intervals. (H) Shows the period required for the cell to migrate ~1 cell length. See Movie S2.

Experiments performed at stage 7. Black arrows show migration direction. Scale bars 5 µm (A, F), 1 µm (B, C).

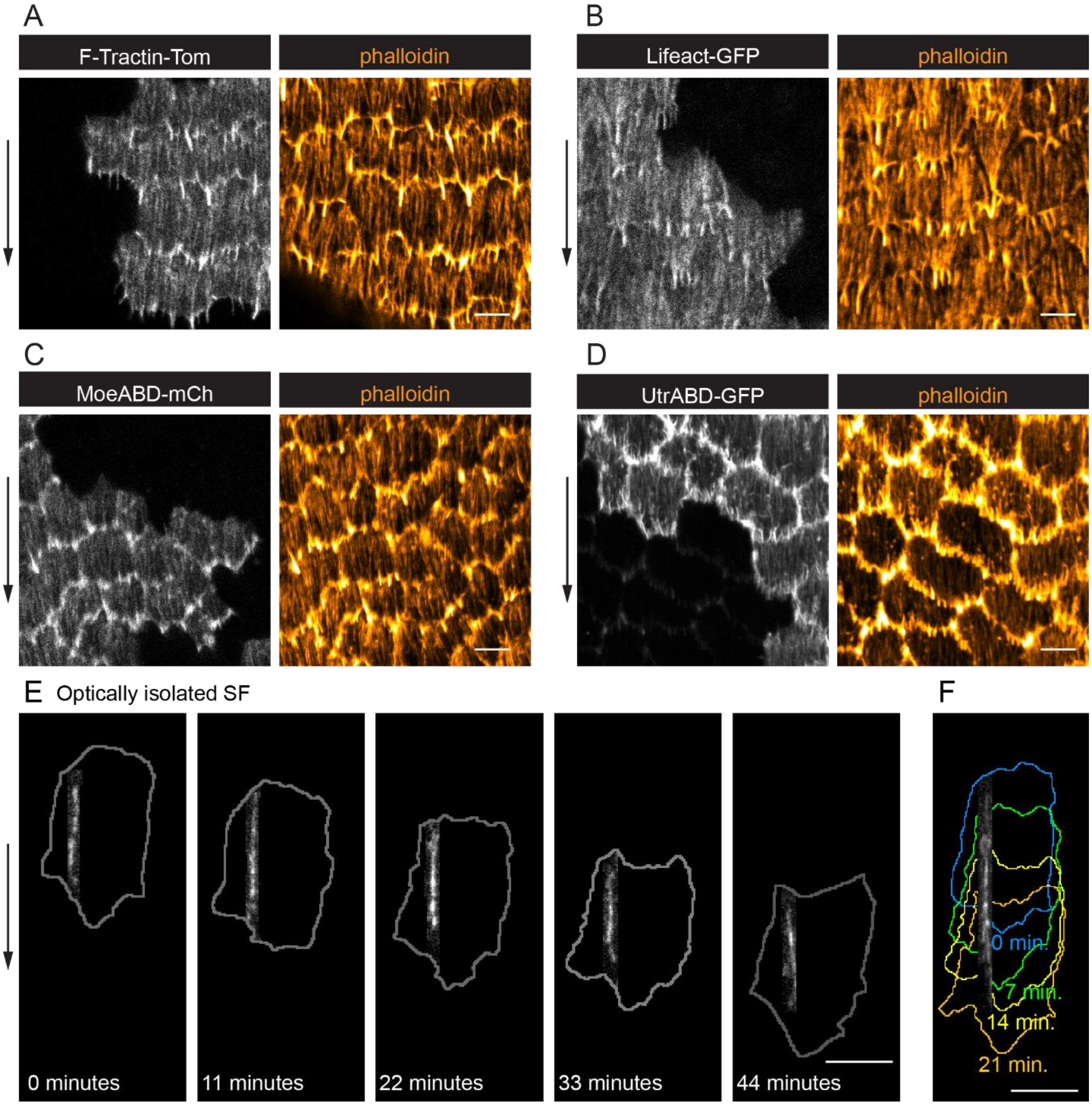

Supplemental Figure 1, related to Figure 2.

(A-D) Images of epithelia with clones of cells expressing live F-actin labels. In all cases, labelling of leading-edge protrusions obscures the ends of the SFs. LifeAct and Utr-ABD (B and D) also significantly alter F-actin organization compared to wild-type cells stained with phalloidin. In D, very weak constitutive expression of Utr is seen outside of clones.

(E) Still images from movie showing an optically isolated SF over 44 minutes; cell outlines are shown in gray.

(F) Maximal projection of the same SF as in (E), shown over 21 minutes; colored cell outlines correspond to time intervals shown.

Experiments performed at stages 7 and 8. Arrows show migration direction. Scale bars 5 µm.

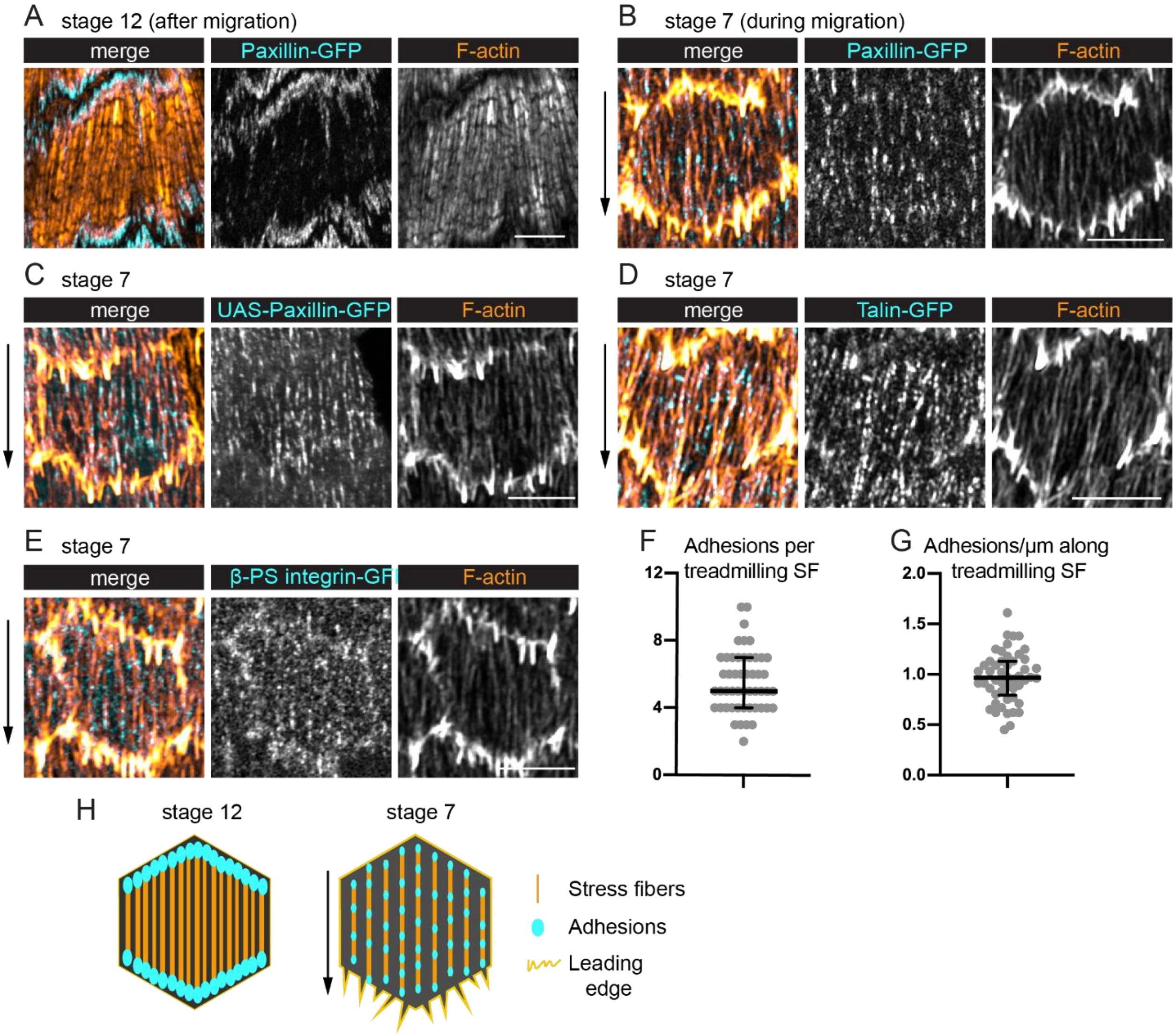

Figure 3. Treadmilling SFs have many adhesions along their lengths

(A, B) Images of SFs in single cells with adhesions labeled with Paxillin-GFP (endogenous tag). (A) After migration stops, there are large adhesions at the ends of SFs. (B) During migration, many smaller adhesions are found along the lengths of the SFs.

(C-E) Images of SFs in single cells showing adhesions labeled with (C) UAS-Paxillin-GFP. (D) Talin-GFP. (E) ß-PS integrin-GFP. Labels in (D, E) are functional endogenously tagged proteins.

(F, G) Quantification of the adhesions associated with individual SFs using Paxillin-GFP. (F) Number. (G) Linear density. n= 277 adhesions from 11 cells in 5 egg chambers. Bars show medians and interquartile ranges.

(H) Illustration of SF structure in post-migratory and migratory cells. Black arrows show migration direction. Scale bars 5 µm.

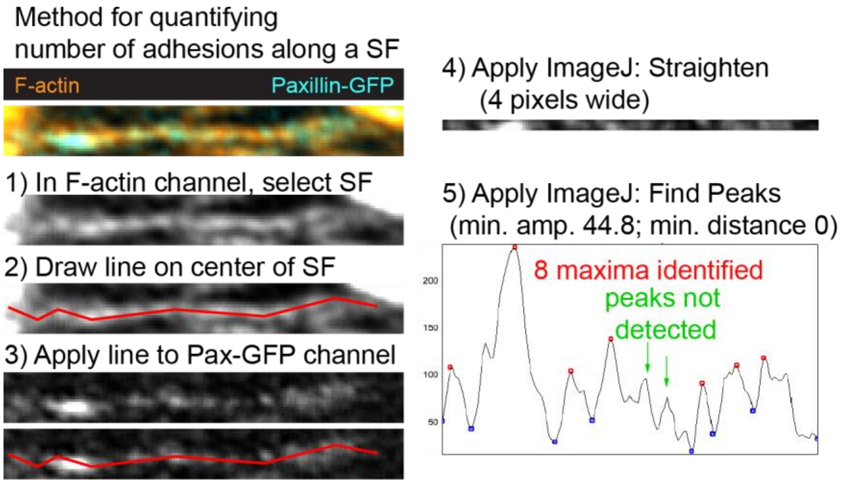

Supplemental Figure 2, related to Figure 3

Method of quantifying number of adhesions along a SF. For the example shown, the method identified 7 peaks (maxima), all of which correspond to easily visible adhesions. Two potential maxima did not meet the threshold for inclusion. These peaks correspond to faint possible adhesions (green arrows), which shows that this method provides a conservative estimate of the number of adhesions along a SF.

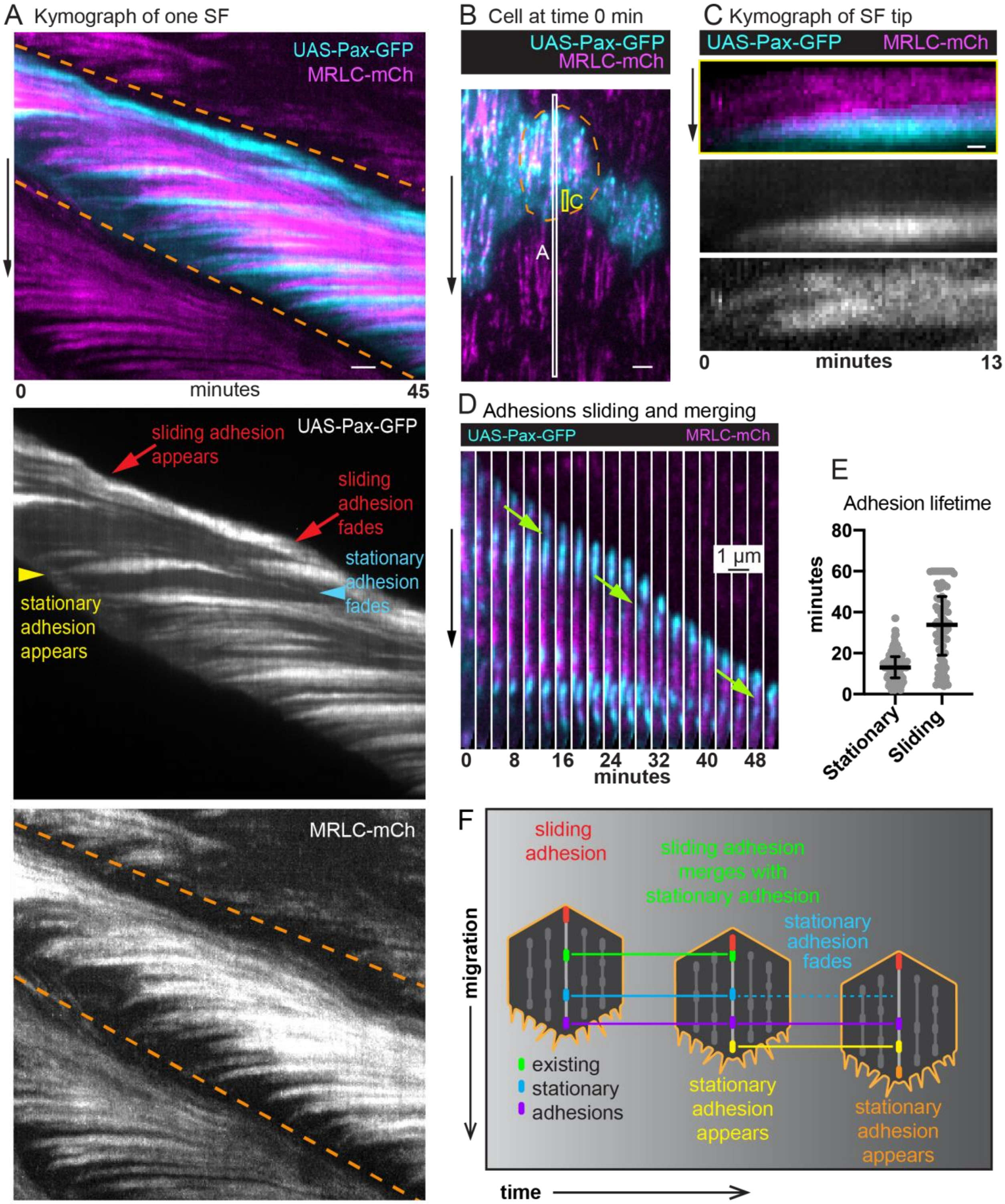

Figure 4. Adhesions are continuously added and removed from treadmilling SFs

(A) Kymograph of one SF (between dashed lines) from the white boxed region in (B) showing addition of new adhesions and actomyosin segments to the tip over time. Yellow arrowhead marks addition of an adhesion that remains stationary relative to cell movement and then fades as the cell's rear approaches (cyan arrowhead). Red arrows highlight the appearance and disappearance of a sliding adhesion at the rear.

(B) Still image from a movie of an epithelium in which all cells express MRLC-mCh and a subset of cells expresses UAS-Paxillin-GFP. Dashed line surrounds one cell. White and yellow boxes correspond to kymographs in (A) and (C), respectively. See Movie S3.

(C) Kymograph of a SF tip from the yellow boxed region in (B), showing that Paxillin-GFP and MRLC-mCh levels increase in synchrony as the SF grows.

(D) Still images from a movie showing a sliding adhesion that persists for at least 50 minutes and merges with three stationary adhesions (green arrows). See Movie S4.

(E) Quantification of adhesion lifetimes. In order on graph, n=134, 84 adhesions from 23 cells in 3 egg chambers. Bars show medians and interquartile ranges.

(F) Illustration summarizing adhesion dynamics in treadmilling SFs.

Experiments performed at stage 7. Black arrows show migration direction. Scale bars 2 µm (A, B), 0.5 µm (C).

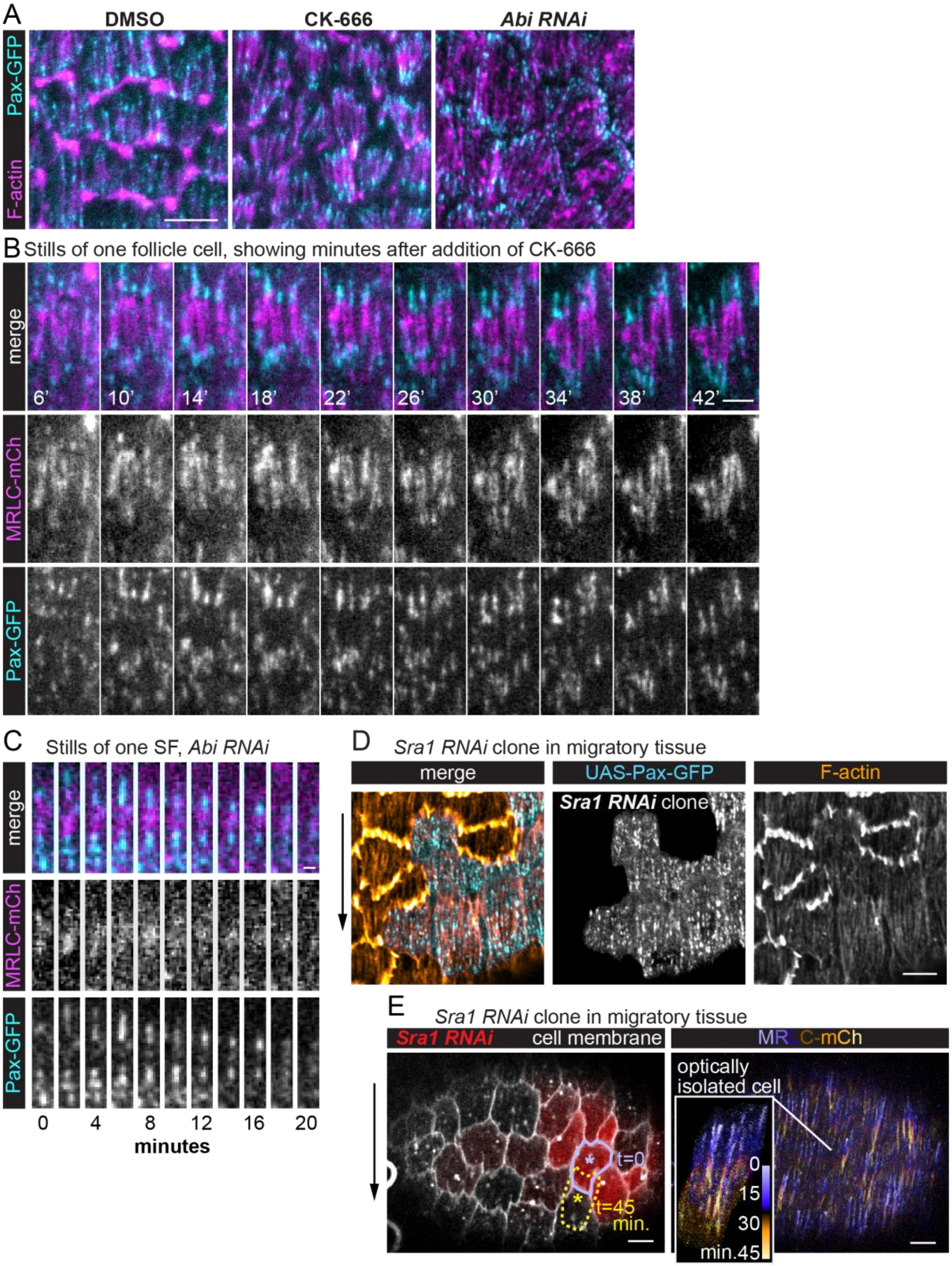

Figure 5. SF treadmilling depends on cell migration

(A) Images of epithelia in which migration has been blocked by eliminating leading edge protrusions. Adhesions become concentrated at the SF ends.

(B) Still images from a movie of one cell showing that internal adhesions disappear, and end adhesions grow as addition of CK-666 slowly brings migration to a stop. See also Movie S5.

(C) Still images from a movie showing one SF in an epithelium in which migration has been blocked. The SF shortens and disappears with no new adhesions added to the ends.

(D) Image of a migrating epithelium with a clone of cells expressing *Sra1 RNAi* to eliminate protrusions. The SFs in the clone maintain internal adhesions.

(E) Still image from a movie of a migrating epithelium with a clone of cells that expresses Sra1-RNAi to eliminate protrusions (left). Outline shows the movement of one cell over 45 minutes (lavender to yellow asterisks). Temporal projection of the SFs in the same epithelium at 20 second intervals (right). Inset shows SF growth in the *Sra1 RNAi* cell marked with the asterisk on the left.

Experiments performed at stage 7. Black arrows show migration direction. Scale bars 5 µm (A, D, E), 1 µm (B), 2 µm (C).

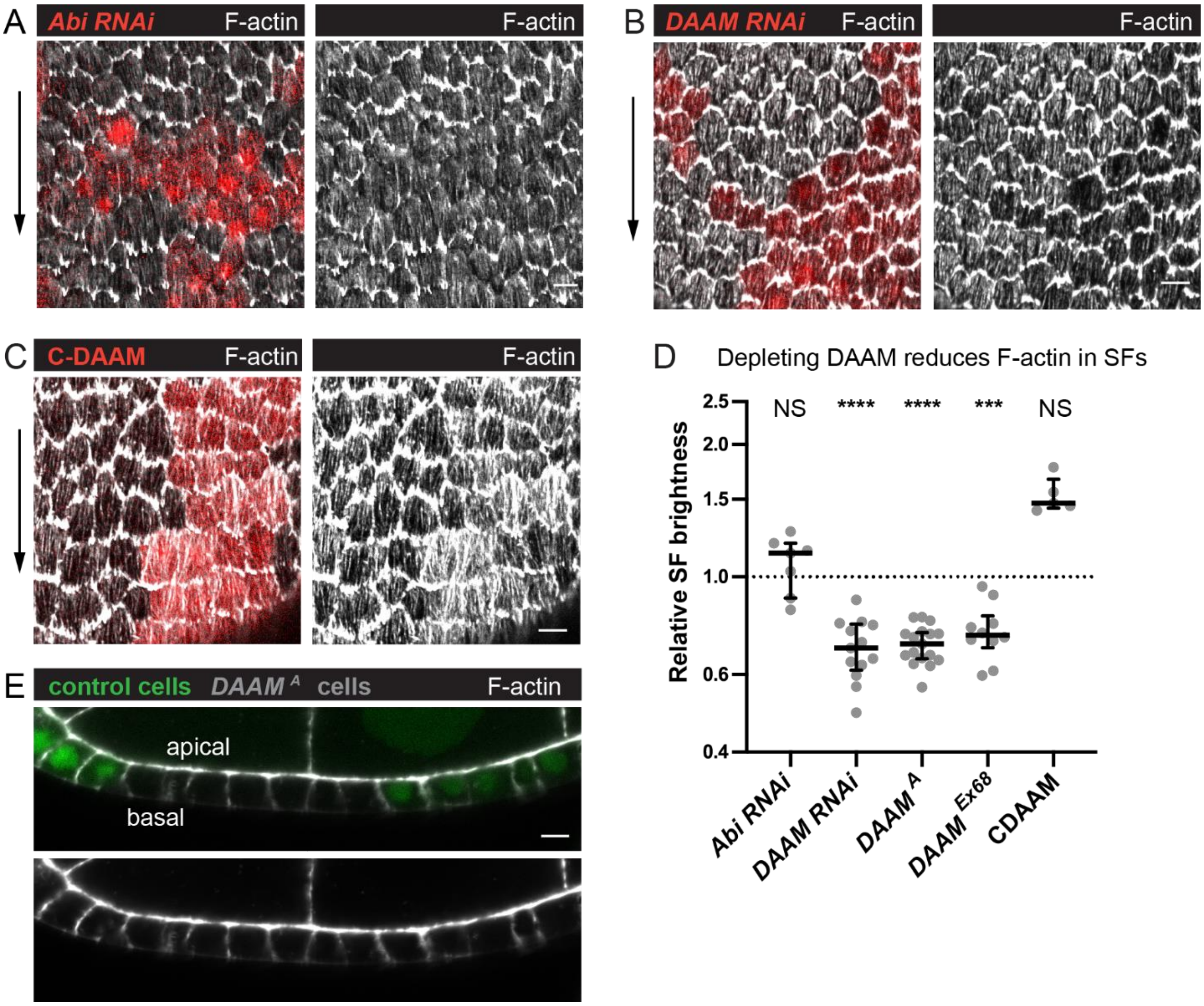

Figure 6. DAAM contributes to treadmilling SF assembly

(A-C) Images of epithelia with clones of cells expressing various transgenes. (A) *Abi RNA*i reduces F-actin in protrusions but not SFs. (B) *DAAM RNAi* reduces SF F-actin. (C) C-DAAM increases SF F-actin.

(D) Quantification of the data in (A-C). Each point is the ratio of the mean value for F-Actin levels in SFs from 10 experimental cells and 10 nearby control cells in the same egg chamber. In order on graph, n=7, 13, 17, 10, 5 egg chambers. Bars show medians and interquartile ranges. Two-tailed Wilcoxon matched pairs signed ranks test. NS (not significant) $p>0.05$, ***$p<0.001$, ****$p<0.0001$.

(E) Image of a transverse section through an epithelium with a clone of *DAAM*^{A} mutant cells. Loss of DAAM does not obviously reduce cortical F-Actin on lateral or apical surfaces.

Experiments performed at stage 7. Black arrows show migration direction. Scale bars 5 µm.

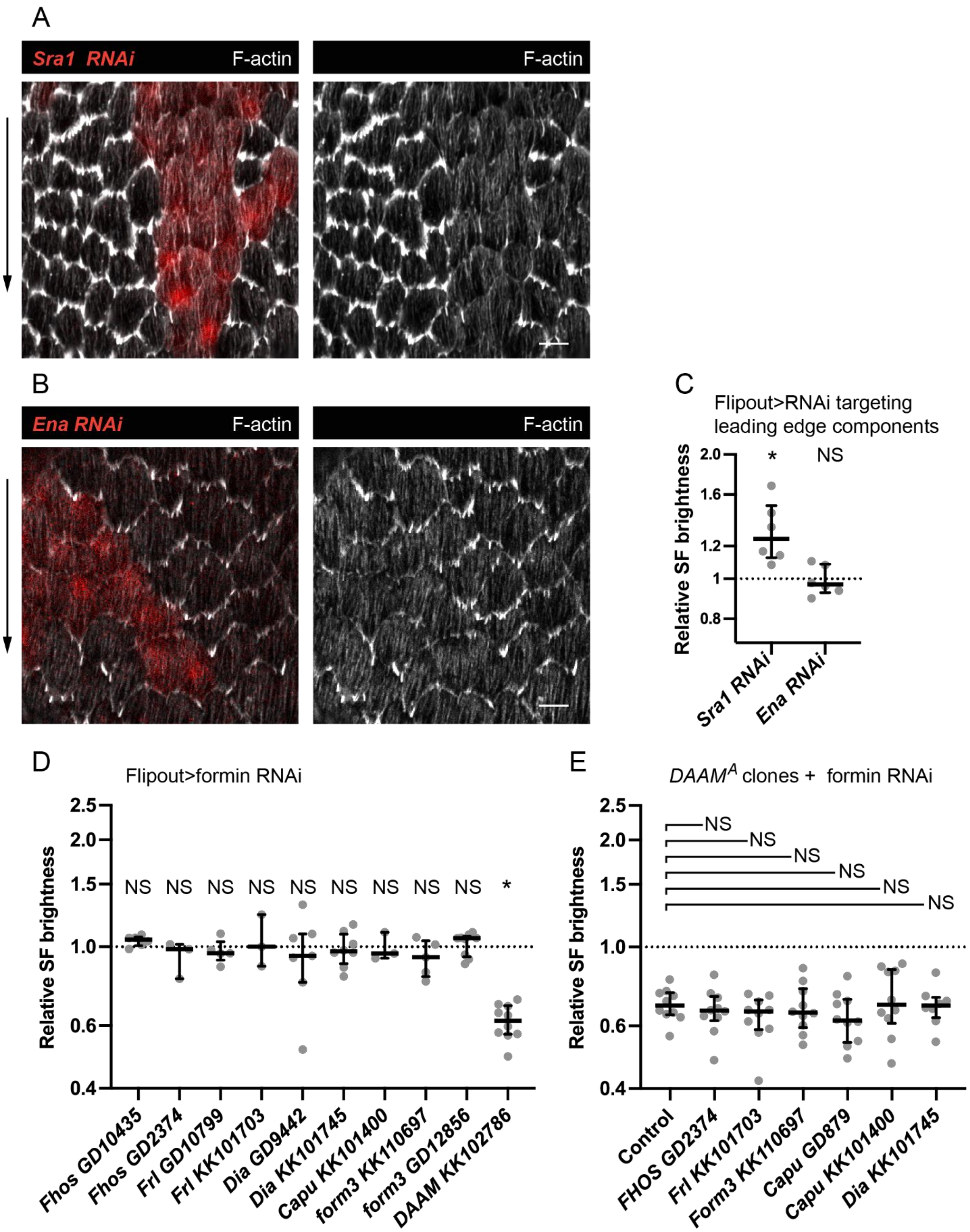

Supplemental Figure 3, related to Figure 6

(A, B) Images of epithelia with clones of cells expressing (A) *Sra1 RNAi* and (B) *Ena RNAi*. F-actin levels are reduced in leading edge protrusions but not in SFs.

(C) Quantification of the data in (A, B). F-actin levels in SFs are the same or higher than controls for both conditions. In order on graph, n=6, 6 egg chambers.

(D) Quantification of SF F-actin levels in clones of cells expressing RNAi against various formins. In order on graph, n=6, 3, 5, 3, 7, 8, 3, 5, 9, 10 egg chambers.

(E) Quantification of SF F-actin levels in *DAAM* mutant clones that are within epithelia that also express RNAi against various formins. In order on graph, n=10, 10, 10, 10, 10, 10, 8 egg chambers.

Experiments performed at stage 7. Black arrows show migration direction. Scale bars 5 µm. (C-E) Each point is the ratio of the mean value for F-Actin levels in SFs from 10 experimental cells and 10 control cells in the same egg chamber. Bars show medians and interquartile ranges. NS (not significant) $p>0.05$, *$p<0.05$. (C, D) Two-tailed Wilcoxon matched pairs signed ranks test. (E) Two-tailed Mann-Whitney compared to control.

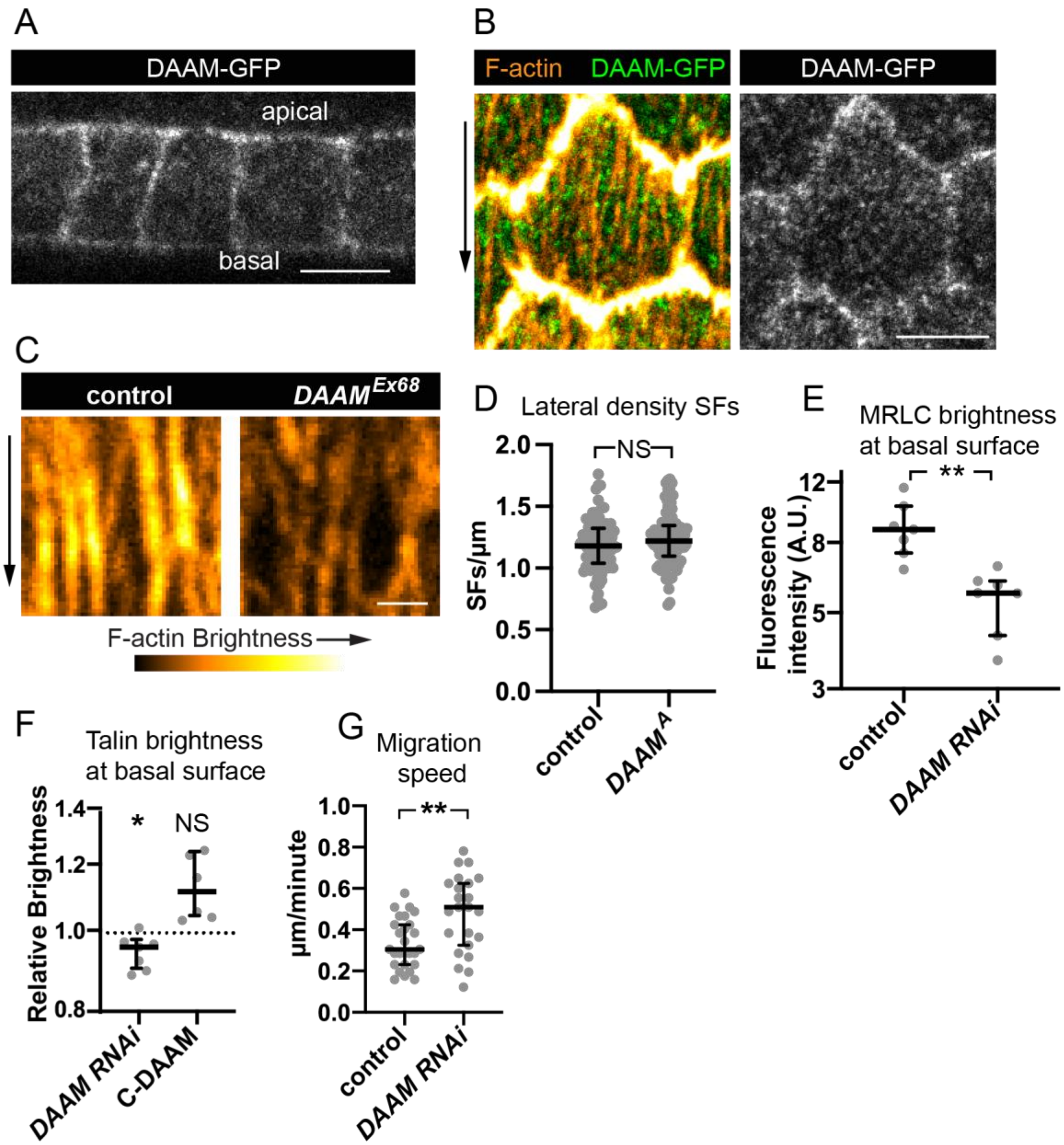

Figure 7. DAAM localizes to the cortex and likely strengthens cell-ECM adhesion via SFs

(A-B) Images of DAAM-GFP (endogenous tag). (A) Transverse section showing that DAAM localizes to the entire cell cortex. (B) Basal view of one cell showing DAAM relative to SFs.

(C) Images of SFs from a control cell and *DAAM*^{Ex86} cell in the same epithelium stained with phalloidin. SFs in *DAAM*^{Ex86} cells are similar in number but have reduced F-actin fluorescence.

(D) Quantification showing that lateral SF density is normal in *DAAM*^{A} cells. In order on graph, n=90, 90 cells from 9 egg chambers with mitotic clones.

(E) Quantification showing that MRLC levels are reduced in *DAAM RNAi* cells. In order on graph, n=7, 7 egg chambers

(F) Quantification showing that Talin levels are reduced in *DAAM RNAi* cells. Each point is the ratio of the mean value for Talin levels from 10 experimental cells and 10 control cells in the same egg chamber. In order on graph, n=7, 6 egg chambers.

(G) Quantification of migration rates for control and *DAAM RNA*i epithelia. In order on graph, n=27, 23 egg chambers.

Experiments performed at stage 7. Black arrows show migration direction. Scale bars, 5 µm (A-B), 1 µm (C). (E-H) Bars show medians and interquartile ranges. NS (not significant) $p>0.05$, $^*p<0.05$, $^{**}p < 0.01$. (D, E, G) Two-tailed Mann-Whitney test. (F) Two-tailed Wilcoxon matched pairs signed ranks test.

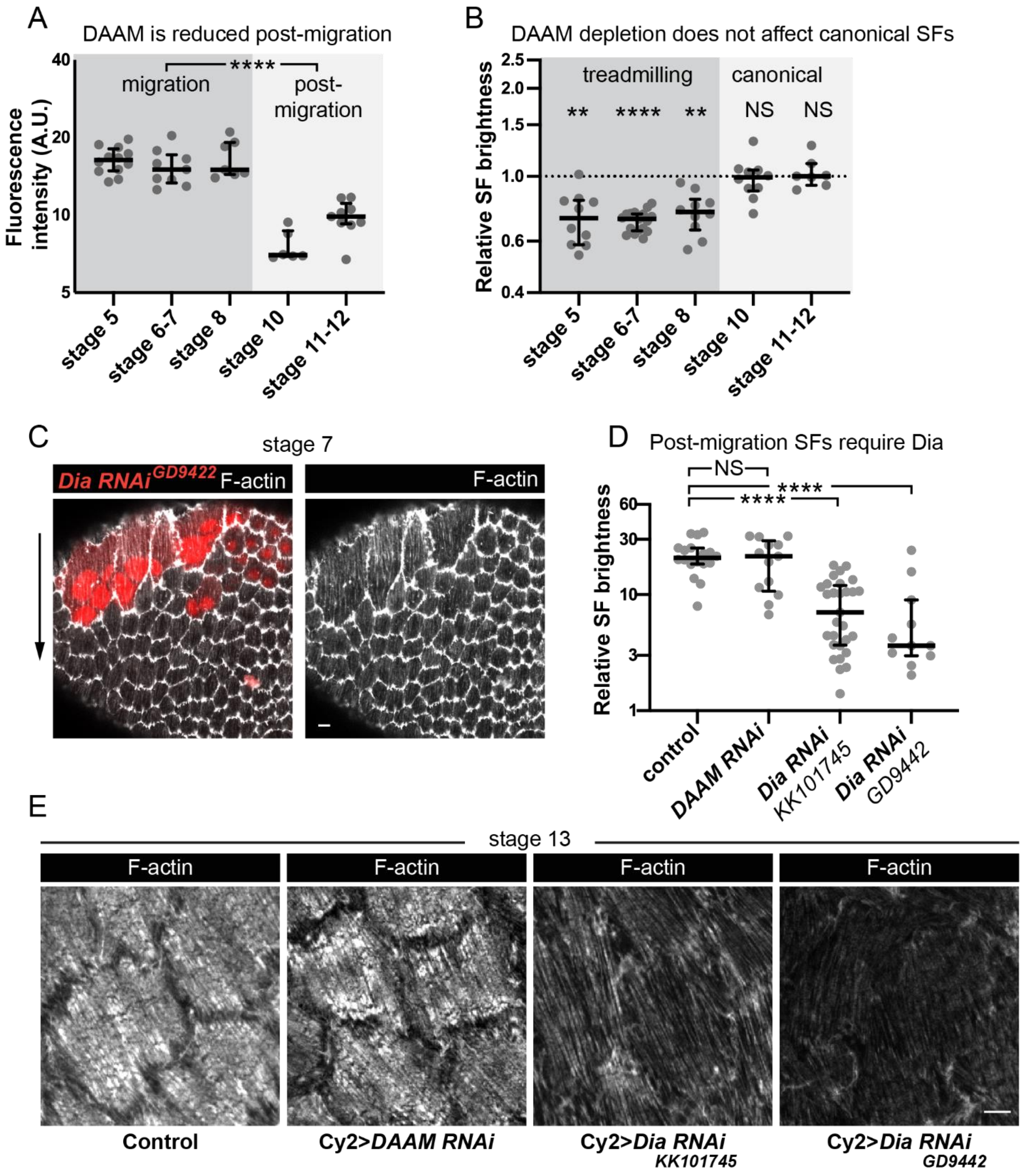

Figure 8. Different formins contribute to treadmilling vs. canonical SFs

(A) Quantification of DAAM-GFP levels at basal surface. Levels are higher during migration stages. In order on graph, n=12, 9, 7, 6, 9 egg chambers. Statistics are on pooled data from migration vs. post-migration stages. Two-tailed Mann-Whitney test.

(B) Quantification of F-actin levels in SFs. *DAAM RNAi* reduces F-actin in treadmilling SFs, but not canonical SFs. Each point is the ratio of the mean value for 10 RNAi cells and 10 control cells in the same egg chamber. In order on graph, n=10, 17, 10, 10, 7 egg chambers. Statistics by stage are two-tailed Wilcoxon matched pairs signed ranks tests. Pooled data from treadmilling vs. canonical SFs is from a two-tailed Mann-Whitney test.

(C) Image of an epithelium with a clone of cells expressing *Dia RNAi*. *Dia RNAi* cells have cytokinesis defects shown by multiple red nuclei per cell, but F-actin levels in SFs are normal.

(D) Quantification of F-actin levels in SFs at stage 13. When Cy2-Gal4 is used to drive RNAi during post-migration stages, *Dia RNAi* reduces F-actin in SFs, but *DAAM RNAi* does not. In order on graph, n=18, 13, 29, 11 egg chambers. Two-tailed Mann-Whitney tests.

(E) Images of cells showing that *Dia RNAi* reduces F-actin levels in SFs post-migration while *DAAM RNAi* does not (images selected from intermediate brightness values measured in D).

Scale bars 5 µm. (A, B, D) Bars show medians and interquartile ranges. NS (not significant) $p>0.05$, $^{**}p<0.01$, $^{****}p<0.0001$

Movie S1 (associated with Figure 2). Timelapse (near-TIRF) of a field of follicle cells with plasma membranes labeled with CellMask and SFs labelled with MRLC-GFP. Note that individual SFs persist as the cells migrate. Imaged at 1 frame/20 sec.

Movie S2 (associated with Figure 2F). Timelapse (near-TIRF) of an optically isolated follicle cell with SFs labelled with MRLC-GFP. Note MRLC-GFP being added to the tips of existing SFs as the cell migrates. Imaged at 1 frame/20 sec.

Movie S3 (associated with Figure 4B). Timelapse (near-TIRF) of a field of follicle cells. The SFs are labelled in all cells with MRLC-mCh. Adhesions are labelled in a subset of cells by da-Gal4 driving patchy expression of UAS-Pax-GFP. Imaged at 1 frame/10 sec, rotated 14 degrees.

Movie S4 (associated with Figure 4D). Timelapse (near-TIRF) of one SF in which myosin is labelled with MRLC-mCh and adhesions labelled with UAS-Pax-GFP. Note the sliding behavior of the final adhesions. Imaged at 1 frame/10 sec, rotated 14 degrees.

Movie S5 (associated with Figure 5B). Timelapse (near-TIRF) of one follicle cell in which SFs are labelled with MRCL-mCh and adhesions labelled with endogenously tagged Pax-GFP. Treatment with the arp2/3 inhibitor CK-666 causes adhesions to become concentrated at SF ends. The time shown reflects minutes after addition of CK-666 (i.e., movie starts at 6 minutes). Imaged at 1 frame/10 sec, rotated 25 degrees.

Table S1. Experimental genotypes

Figure	**Panel**	**Genotype**	**°C**
1	A-B	*w*^{1118}	25
2	A-C, F-I	*sqh*^{Ax3}*/w;; sqh-GFP*	25
	D-E	*sqh*^{Ax3}*/w; UAS-Pax-GFP/+; da-Gal4/sqh-mCh*	25
S1	A	*w/y w hsFLP/+;; UAS-Ftractin-Tom/act5c>>Gal4*	25
	B	*y w/y w hsFLP;; UAS-Lifeact-GFP/+; act5c>>Gal4/+*	25
	C	*w/y w hsFLP;; UAS-Moe-ABD-mCh/ act5c>>Gal4*	25
	D	*w/y w hsFLP; UAS-Utr-ABD-GFP/+; act5c>>Gal4/+*	25
	E-F	*sqh*^{Ax3}*/w;; sqh-GFP*	25
3	A-B, F-H	*w; Pax-GFP*	25
	C	*w/y* w*; tj-Gal4/UAS-Pax-GFP*	25
	D	*w;;Talin-GFP*	25
	E	*w mys-GFP*	25
S2	-	*w; Pax-GFP*	25
4	A-E	*sqh*^{Ax3}*/w; UAS-Pax-GFP/+; da-Gal4/sqh-mCh*	25
5	A left	*w; Pax-GFP/+; sqh-mCh/+*	25
	A middle, B	*w; Pax-GFP/+; sqh-mCh/+*	25
	A right, C	*w/y w; tj-Gal4/Pax-GFP; sqh-mCh/UAS-Abi RNAi*$^{NIG:\ 9749R\text{-}3}$	25
	D	*y sc* v sev/y w hsFLP; UAS-Pax-GFP/ +; UAS-Sra1 RNAi*$^{TRiP.HMS01754}$*/act5c>>Gal4*	25
	E	*y sc* v sev/y w hsFLP; act5c>>Gal4, UAS-RFP/+; UAS-Sra1 RNAi*$^{TRiP.HMS01754}$*/sqh-mCh*	25
6	A, D	*w/y w hsFLP;; UAS-Abi RNAi*$^{NIG:\ 9749R\text{-}3}$*/act5c>>Gal4, UAS-RFP*	25
	B, D	*w/y w hsFLP; UAS-DAAM RNAi*^{KK102786}*/+; act5c>>Gal4, UAS-RFP/+*	25
	C, D	*w/y w hsFLP;; UAS-pTWFlag-C-DAAM/+; act5c>>Gal4, UAS-RFP/+*	29 (2d)
	D	*hsFLP Ubi-mRFP-nls FRT19A/DAAM*^{A} *FRT19A*	25
	D	*hsFLP Ubi-mRFP-nls FRT19A/DAAM*^{Ex68} *FRT19A*	25

Figure	**Panel**	**Genotype**	**°C**
	E	*hsFLP Ubi-mRFP-nls FRT19A/DAAM*^{A} *FRT19A*	25
S3	A, C	*y sc* v sev/y w hsFLP;; UAS-Sra1* *RNAi*$^{TRiP.HMS01754}$*/act5c>>Gal4, UAS-RFP*	25
	B, C	*w/y w hsFLP; UAS-Ena RNAi*^{GD8910}*/+; act5c>>Gal4, UAS-RFP/+*	25
	D	*w/y w hsFLP; UAS-RNAi /+; act5c>>Gal4, UAS-RFP/+* *or w/y w hsFLP;; UAS-RNAi/act5c>>Gal4, UAS-RFP* *(exact RNAi lines used are noted in figure)*	29 (2d)
	E	*Ubi-mRFP-nls FRT19A/DAAM*^{A} *FRT19A; tj-Gal4, UAS-Flp/* *UAS-RNAi or* *Ubi-mRFP-nls FRT19A/DAAM*^{A} *FRT19A; tj-Gal4, UAS-Flp/+;* *UAS-RNAi/+* *(exact RNAi lines used are noted in figure)*	25
7	A, B	*DAAM-GFP/w*^{1118}	25
	C	*DAAM*^{Ex68} *FRT19A/hsFLP Ubi-mRFP-nls FRT19A*	25
	D	*DAAM*^{A} *FRT19A/hsFLP Ubi-mRFP-nls FRT19A; tj-Gal4/+*	25
	E control	*w/y w; Cyo/UAS-DAAM RNAi*^{KK102786}*; sqh-mCh/+*	25
	E experimental	*w/y w; tj-Gal4/UAS-DAAM-DAAM RNAi*^{KK102786}*; sqh-mCh/+*	25
	F depletion	*w/y w hsFLP; UAS-DAAM RNAi*^{KK102786}*; TalinGFP/act5c>>Gal4, UAS-RFP*	29 (2d)
	F overexpression	*w/y w hsFLP; UAS-pTWFlag-C-DAAM/+;* *TalinGFP/act5c>>Gal4, UAS-RFP*	25
	G control	*w/y w; tj-Gal4/+; UAS-Dcr2/+*	25
	G experimental	*w/y w; tj-Gal4; UAS-Dcr2/UAS-DAAM RNAi*^{KK102786}	25
8	A	*DAAM-GFP/w*^{1118}	25
	B	*DAAM*^{A} *FRT19A/hsFLP Ubi-mRFP-nls FRT19A* *and DAAM*^{Ex68} *FRT19A/hsFLP Ubi-mRFP-nls FRT19A*	25
	C	*w/y w hsFLP; +; UAS-Dia RNAi*^{GD9442}*/act5c>>Gal4, UAS-nls-RFP*	25
	D	*(same as the four genotypes listed in 8E below)*	29 (2d)
	E left	*w*^{1118}*; Cy2-Gal4/+*	29 (2d)
	E left middle	*w*^{1118}*; Cy2-Gal4/UAS-DAAM RNAi*^{KK102786}	29 (2d)

Figure	**Panel**	**Genotype**	**°C**
	E right middle	w^{1118}; *Cy2-Gal4/+; UAS-Dia RNAi*^{KK101745}	29 (2d)
	E right	w^{1118}; *Cy2-Gal4/+; UAS-Dia RNAi*^{GD9442}	29 (2d)
Movies	S1, S2	*sqh*^{Ax3}*/w;; sqh-GFP*	25
	S3, S4	*sqh*^{Ax3}*/w; UAS-Pax-GFP/+; da-Gal4/sqh-mCh*	25
	S5	*w; Pax-GFP/+; sqh-mCh/+*	25

KEY RESOURCES

Reagent type (species) or resource	**Designation**	**Sources or reference**	**Identifiers**	**Additional information**
Antibody	rabbit polyclonal anti-GFP directly coupled to Alexa Fluor 488	Invitrogen	Cat # A21311	1:400
Chemical compound, drug	CellMaskTM Deep Red Plasma Membrane Stain	Thermo Fisher Scientific	Cat# C10046	1:1000
Chemical compound, drug	Alexa FluorTM 647 phalloidin	Thermo Fisher Scientific	Cat# A22287	1:100
Chemical compound, drug	Alexa FluorTM 488 phalloidin	Thermo Fisher Scientific	Cat# A12379	1:200
Chemical compound, drug	Scheider’s Drosophila medium	Thermo Fisher Scientific	Cat# 21720-024	
Chemical compound, drug	Fetal Bovine Serum	Gibco	Cat# 10438-018	
Chemical compound, drug	Recombinant Human Insulin	Millipore Sigma	Cat# 12643	
Other	Soda Lime Glass Beads, 48-51 µm	Cospheric LLC	Cat# S-SLGMS-2.5	
Chemical compound, drug	Formaldehyde, 16%, methanol free, Ultra-Pure	Polysciences	Cat# 18814-10	
Chemical compound, drug	SlowFadeTM Diamond Antifade mounting medium	Invitrogen	Cat# S36972	
Chemical compound, drug	SlowFadeTM Antifade Kit	Thermo Fisher Scientific	Cat# S2828	
Chemical compound, drug	CK-666	Millipore Sigma	Cat# SML0006	
software, algorithm	ImageJ version 2.1.0/1.53c		https://fiji.sc/	
software, algorithm	Handbrake 1.3.3 The open source video transcoder	HandBrake Team	https://handbrake.fr/	
software, algorithm	Zen Blue	Zeiss		
software, algorithm	Zen Black	Zeiss		
software, algorithm	MetaMorph	Molecular Devices		

KEY RESOURCES

software, algorithm	Prism Version 8	Graphpad		
Drosophila: Standard control strain: w^{1118}	w[1118]	Bloomington Drosophila Stock Center	BDSC: 3605; FlyBase ID: FBst0003605	
Drosophlia: sqh-GFP	Sqh-2xTY1- SGFP-3xFLAG	Vienna Drosophila Resource Center	VDRC: 318484	
Drosophila: MRLC-mCh	sqhAx3/FM7;; sqh>sqh-mCh/TM3, Ser, actGFP	Laboratory of Eric Wieschaus (Martin et al. 2009)		
Drosophila: UAS-Pax-GFP	UAS-Pax-GFP	Laboratory of Denise Montell (He et al. 2010)		
Drosophila: daughterless Gal4	w*; P{GAL4-da.G32}UH1, Sb1/TM6B, Tb1	Bloomington Drosophila Stock Center	BDSC: 31418; FlyBaseID: FBst0055851	
Drosophila: hsFLP	P{ry[+t7.2] = hsFLP}22, w[*]}	Bloomington Drosophila Stock Center	BDSC: 8862; FlyBase ID: FBst0008862	
Drosophila: act5c>>Gal4	y1 w*; P{GAL4-Act5C(FRT.CD2).P}S	Bloomington Drosophila Stock Center	BDSC: 4780; FlyBase ID: FBst0004780	
Drosophila: UAS-Ftractin-Tom	P{UASp-F-Tractin.tdTomato}15A/SM6b; MKRS/TM2	Bloomington Drosophila Stock Center	BDSC: 58989; FlyBaseID: FBtp0095457	
Drosophila: UAS-Lifeact-GFP	y w; UAS-Lifeact-GFP	Bloomington Drosophila Stock Center	BDSC: 35544; FlyBaseID: FBst0035544	
Drosophila: UAS-MoesinABD—mCh 42c	UASMoesinABD—mCh 42c	Laboratory of Brooke McCartney		
Drosophila: UAS-Utr-ABD-GFP	UAS-Utrophin-ABD-GFP	Laboratory of Thomas Lecuit (Rauzi et al. 2010)		
Drosophila: Pax-GFP	w[1118]; PBac{EGFP-IV}Pax[KM0601]	Kyoto Stock Center	DGRC: 109971	

KEY RESOURCES

Drosophila: Talin-GFP	y w; rhea-eGFP-Flash-Strep-FLAG/TM6b	Laboratory of Hugo Bellen (Venken et al. 2011)		
Drosophila: Mys-GFP	Mys-GFP	Laboratory of Nicholas Brown (Klapholtz et al. 2015)		
Drosophila: traffic jam-Gal4	y* w*; P{w+mW.hs=GawB}NP1624 / CyO, P{w- =UASlacZ.UW14}UW14	Kyoto Stock Center	DGRC: 104055	
Drosophila: RNAi of Abi	UAS-Abi RNAi	National Institute of Genetics, Japan	NIG: 9749R-3	
Drosophila: RNAi of Sra1	y1 sc* v1 sev21; P{TRiP.HMS01754}attP2	Bloomington Drosophila Stock Center	BDSC: 38294; FlyBaseID: FBst0038294	
Drosophila: act5c>>Gal4, UAS-RFP	D. melanogaster. w[1118]; P{w[+mC]=GAL4-Act5C(FRT.CD2).P}S, P{w[+mC]=UAS-RFP.W}3/TM3, Sb[1]	Bloomington Drosophila Stock Center	BDSC: 30558; FlyBase ID: FBst0030558	
Drosophila: UAS-C-DAAM	UAS-pTWFlag-C-DAAM	Laboratory of József. Mihály (Matusek et al. 2006)		
Drosophila: hsFLP RFP FRT 19A	Ubi-mRFP.nls, w*, hsFLP neoFRT19A	Bloomington Drosophila Stock Center	BDSC: 31418; FlyBaseID: FBst0031418	
Drosophila: DAAMA FRT 19A	y1 DAAMA w* P{neoFRT}19A/FM7c, P{GAL4-Kr.C}DC1, P{UAS-GFP.S65T}DC5, sn+	Bloomington Drosophila Stock Center	BDSC: 52348; FlyBaseID: FBst0052348	
Drosophila: DAAMEx68	DAAMEx68	Laboratory of József. Mihály (Dollar et al. 2016)		
Drosophila: 19A FRT	P{ry[+t7.2]=neoFRT}19A; ry[506]	Bloomington Drosophila Stock Center	BDSC: 1709; FlyBaseID: FBst0001709	

KEY RESOURCES

Drosophila: DAAMEx68 FRT 19A	DAAMEx68 FRT 19A	Recombination only, this study	DAAMEx68 from J. Mihály; and 19A FRT from BDSC: 1709	
Drosophila: RFP FRT 19A	P{w[+mC]=Ubi-mRFP.nls}1, w[1118], P{ry[+t7.2]=neoFRT}19A	Bloomington Drosophila Stock Center	BDSC: 31416; FlyBase ID: FBst0031416	
Drosophila: RNAi of DAAM	w[1118]; P{KK102786}v103921	Vienna Drosophila Resource Center	VDRC: 103921	
Drosphila: RNAi of Dia	w[1118]; P{KK101745}v103914	Vienna Drosophila Resource Center	VDRC: 103914	
Drosophila: RNAi of Dia	w[1118]; P{GD9442}v20518	Vienna Drosophila Resource Center	VDRC: 20518	
Drosophila: RNAi of FHOS/Knittrig	w[1118]; +; P{GD10435}v145838	Vienna Drosophila Resource Center	VDRC: 45838 (line has been discontinued)	
Drosophila: RNAi of FHOS/Knittrig	w[1118]; P{GD2374}v34034	Vienna Drosophila Resource Center	VDRC: 34034	
Drosophila: RNAi of Frl	w[1118]; +; P{GD10799}v34413	Vienna Drosophila Resource Center	VDRC: 34413	
Drosophila: RNAi of Frl	w[1118]; P{KK101703}v110438	Vienna Drosophila Resource Center	VDRC: 110438	
Drosophila: RNAi of Capu	w[1118]; P{KK101400}v110404	Vienna Drosophila Resource Center	VDRC: 110404	
Drosophila: RNAi of Capu	w[1118]; P{GD879}v34278	Vienna Drosophila Resource Center	VDRC: 34278	
Drosophila: RNAi of Form3	w[1118]; P{GD12856}v 45594	Vienna Drosophila Resource Center	VDRC: 45594	
Drosophila: RNAi of Form3	w[1118]; P{KK110697}v107473	Vienna Drosophila Resource Center	VDRC: 107473	

KEY RESOURCES

Drosophila: RNAi of Ena	w[1118]; P{GD8910}v43058	Vienna Drosophila Resource Center	VDRC: 43058	
Drosophila: DAAM-GFP	w[1118] DAAM-GFP	Laboratory of József. Mihály (Molnár et al. 2014)		
Drosophila: UAS-Dcr	w[1118]; P{w[+mC] = UAS-Dcr-2.D}10	Bloomington Drosophila Stock Center	BDSC: 24651; FlyBase ID: FBst0024651	
Drosophila: Cy2 Gal4	w[1118]; Cy-Gal4	Laboratory of Nir Yakoby (Queenan et al.1997)	FBti0007266	

755

REFERENCES

Ballestrem, C., Hinz, B., Imhof, B.A., Wehrle-Haller, B., 2001. Marching at the front and dragging behind: differential alphaVbeta3-integrin turnover regulates focal adhesion behavior. J. Cell Biol. 155, 1319–1332. https://doi.org/10.1083/jcb.200107107

Barlan, K., Cetera, M., Horne-Badovinac, S., 2017. Fat2 and Lar Define a Basally Localized Planar Signaling System Controlling Collective Cell Migration. Dev. Cell 40, 467-477.e5. https://doi.org/10.1016/j.devcel.2017.02.003

Burridge, K., Guilluy, C., 2016. Focal adhesions, stress fibers and mechanical tension. Exp. Cell Res. 343, 14–20. https://doi.org/10.1016/j.yexcr.2015.10.029

Burridge, K., Wittchen, E.S., 2013. The tension mounts: Stress fibers as force-generating mechanotransducers. J Cell Biol 200, 9–19. https://doi.org/10.1083/jcb.201210090

Campos, F.C., Dennis, C., Alégot, H., Fritsch, C., Isabella, A., Pouchin, P., Bardot, O., Horne-Badovinac, S., Mirouse, V., 2020. Oriented basement membrane fibrils provide a memory for F-actin planar polarization via the Dystrophin-Dystroglycan complex during tissue elongation. Development 147. https://doi.org/10.1242/dev.186957

Cetera, M., Horne-Badovinac, S., 2015. Round and round gets you somewhere: collective cell migration and planar polarity in elongating Drosophila egg chambers. Curr. Opin. Genet. Dev. 32, 10–15. https://doi.org/10.1016/j.gde.2015.01.003

Cetera, M., Lewellyn, L., Horne-Badovinac, S., 2016. Cultivation and Live Imaging of Drosophila Ovaries, in: Dahmann, C. (Ed.), Drosophila, Methods in Molecular Biology. Springer New York, New York, NY, pp. 215–226. https://doi.org/10.1007/978-1-4939-6371-3_12

Cetera, M., Ramirez-San Juan, G.R., Oakes, P.W., Lewellyn, L., Fairchild, M.J., Tanentzapf, G., Gardel, M.L., Horne-Badovinac, S., 2014. Epithelial rotation promotes the global alignment of contractile actin bundles during Drosophila egg chamber elongation. Nat. Commun. 5, 5511. https://doi.org/10.1038/ncomms6511

Chugh, P., Paluch, E.K., 2018. The actin cortex at a glance. J. Cell Sci. 131, jcs186254. https://doi.org/10.1242/jcs.186254

Costa, K.D., Hucker, W.J., Yin, F.C.-P., 2002. Buckling of actin stress fibers: A new wrinkle in the cytoskeletal tapestry. Cell Motil. 52, 266–274. https://doi.org/10.1002/cm.10056

Courtemanche, N., 2018. Mechanisms of formin-mediated actin assembly and dynamics. Biophys. Rev. 10, 1553–1569. https://doi.org/10.1007/s12551-018-0468-6

Delon, I., Brown, N.H., 2009. The integrin adhesion complex changes its composition and function during morphogenesis of an epithelium. J. Cell Sci. 122, 4363–4374. https://doi.org/10.1242/jcs.055996

Digman, M.A., Brown, C.M., Horwitz, A.R., Mantulin, W.W., Gratton, E., 2008. Paxillin Dynamics Measured during Adhesion Assembly and Disassembly by Correlation Spectroscopy. Biophys. J. 94, 2819–2831. https://doi.org/10.1529/biophysj.107.104984

Dollar, G., Gombos, R., Barnett, A.A., Sanchez Hernandez, D., Maung, S.M.T., Mihály, J., Jenny, A., 2016. Unique and Overlapping Functions of Formins Frl and DAAM During Ommatidial Rotation and Neuronal Development in Drosophila. Genetics 202, 1135–1151. https://doi.org/10.1534/genetics.115.181438

Friedl, P., Gilmour, D., 2009. Collective cell migration in morphogenesis, regeneration and cancer. Nat. Rev. Mol. Cell Biol. 10, 445–457. https://doi.org/10.1038/nrm2720

Gutzeit, H.O., 1991. Organization and in vitro activity of microfilament bundles associated with the basement membrane of Drosophila follicles. Acta Histochem. Suppl. 41, 201–210.

Gutzeit, H.O., 1990. The microfilament pattern in the somatic follicle cells of mid-vitellogenic ovarian follicles of Drosophila. Eur. J. Cell Biol. 53, 349–356.

Haigo, S.L., Bilder, D., 2011. Global tissue revolutions in a morphogenetic movement controlling elongation. Science 331, 1071–1074. https://doi.org/10.1126/science.1199424

He, L., Wang, X., Tang, H.L., Montell, D.J., 2010. Tissue elongation requires oscillating contractions of a basal actomyosin network. Nat. Cell Biol. 12, 1133–1142. https://doi.org/10.1038/ncb2124

Horne-Badovinac, S., Bilder, D., 2005. Mass transit: Epithelial morphogenesis in the Drosophila egg chamber. Dev. Dyn. 232, 559–574. https://doi.org/10.1002/dvdy.20286

Hotulainen, P., Lappalainen, P., 2006. Stress fibers are generated by two distinct actin assembly mechanisms in motile cells. J. Cell Biol. 173, 383–394. https://doi.org/10.1083/jcb.200511093

Isabella, A.J., Horne-Badovinac, S., 2016. Rab10-mediated secretion synergizes with tissue movement to build a polarized basement membrane architecture for organ morphogenesis. Dev. Cell 38, 47–60. https://doi.org/10.1016/j.devcel.2016.06.009

Jain, S., Ladoux, B., Mège, R.-M., 2021. Mechanical plasticity in collective cell migration. Curr. Opin. Cell Biol. 72, 54–62. https://doi.org/10.1016/j.ceb.2021.04.006

Kassianidou, E., Kumar, S., 2015. A biomechanical perspective on stress fiber structure and function. Biochim. Biophys. Acta 1853, 3065–3074. https://doi.org/10.1016/j.bbamcr.2015.04.006

Katoh, K., Kano, Y., Masuda, M., Onishi, H., Fujiwara, K., 1998. Isolation and Contraction of the Stress Fiber. Mol. Biol. Cell 9, 1919–1938.

Klapholz, B., Herbert, S.L., Wellmann, J., Johnson, R., Parsons, M., Brown, N.H., 2015. Alternative Mechanisms for Talin to Mediate Integrin Function. Curr. Biol. 25, 847–857. https://doi.org/10.1016/j.cub.2015.01.043

Kühn, S., Geyer, M., 2014. Formins as effector proteins of Rho GTPases. Small GTPases 5, e983876. https://doi.org/10.4161/sgtp.29513

Laukaitis, C.M., Webb, D.J., Donais, K., Horwitz, A.F., 2001. Differential Dynamics of α5 Integrin, Paxillin, and α-Actinin during Formation and Disassembly of Adhesions in Migrating Cells. J. Cell Biol. 153, 1427–1440. https://doi.org/10.1083/jcb.153.7.1427

Lehtimäki, J., Hakala, M., Lappalainen, P., 2017. Actin Filament Structures in Migrating Cells, in: Jockusch, B.M. (Ed.), The Actin Cytoskeleton, Handbook of Experimental Pharmacology. Springer International Publishing, Cham, pp. 123–152. https://doi.org/10.1007/164_2016_28

Lehtimäki, J.I., Rajakylä, E.K., Tojkander, S., Lappalainen, P., 2021. Generation of stress fibers through myosin-driven re-organization of the actin cortex. eLife 10, e60710. https://doi.org/10.7554/eLife.60710

Lewellyn, L., Cetera, M., Horne-Badovinac, S., 2013. Misshapen decreases integrin levels to promote epithelial motility and planar polarity in Drosophila. J. Cell Biol. 200, 721–729. https://doi.org/10.1083/jcb.201209129

Livne, A., Geiger, B., 2016. The inner workings of stress fibers - from contractile machinery to focal adhesions and back. J. Cell Sci. 129, 1293–1304. https://doi.org/10.1242/jcs.180927

Lu, J., Doyle, A.D., Shinsato, Y., Wang, S., Bodendorfer, M.A., Zheng, M., Yamada, K.M., 2020. Basement Membrane Regulates Fibronectin Organization Using Sliding Focal Adhesions Driven by a Contractile Winch. Dev. Cell. https://doi.org/10.1016/j.devcel.2020.01.007

Martin, A.C., Kaschube, M., Wieschaus, E.F., 2009. Pulsed contractions of an actin-myosin network drive apical constriction. Nature 457, 495–499. https://doi.org/10.1038/nature07522

Matusek, T., Djiane, A., Jankovics, F., Brunner, D., Mlodzik, M., Mihály, J., 2006. The Drosophila formin DAAM regulates the tracheal cuticle pattern through organizing the actin cytoskeleton. Dev. Camb. Engl. 133, 957–966. https://doi.org/10.1242/dev.02266

Mishra, A.K., Campanale, J.P., Mondo, J.A., Montell, D.J., 2019. Cell interactions in collective cell migration. Development 146. https://doi.org/10.1242/dev.172056

Molnár, I., Migh, E., Szikora, S., Kalmár, T., Végh, A.G., Deák, F., Barkó, S., Bugyi, B., Orfanos, Z., Kovács, J., Juhász, G., Váró, G., Nyitrai, M., Sparrow, J., Mihály, J., 2014. DAAM is required for thin filament formation and Sarcomerogenesis during muscle development in Drosophila. PLoS Genet. 10, e1004166. https://doi.org/10.1371/journal.pgen.1004166

Naumanen, P., Lappalainen, P., Hotulainen, P., 2008. Mechanisms of actin stress fibre assembly. J. Microsc. 231, 446–454. https://doi.org/10.1111/j.1365-2818.2008.02057.x

Oakes, P.W., Beckham, Y., Stricker, J., Gardel, M.L., 2012. Tension is required but not sufficient for focal adhesion maturation without a stress fiber template. J. Cell Biol. 196, 363–374. https://doi.org/10.1083/jcb.201107042

Popkova, A., Stone, O.J., Chen, L., Qin, X., Liu, C., Liu, J., Belguise, K., Montell, D.J., Hahn, K.M., Rauzi, M., Wang, X., 2020. A Cdc42-mediated supracellular network drives polarized forces and Drosophila egg chamber extension. Nat. Commun. 11, 1–15. https://doi.org/10.1038/s41467-020-15593-2

Queenan, A.M., Ghabrial, A., Schüpbach, T., 1997. Ectopic activation of torpedo/Egfr, a Drosophila receptor tyrosine kinase, dorsalizes both the eggshell and the embryo. Dev. Camb. Engl. 124, 3871–3880.

Rauzi, M., Lenne, P.-F., Lecuit, T., 2010. Planar polarized actomyosin contractile flows control epithelial junction remodelling. Nature 468, 1110–1114. https://doi.org/10.1038/nature09566

Rid, R., Schiefermeier, N., Grigoriev, I., Small, J.V., Kaverina, I., 2005. The last but not the least: The origin and significance of trailing adhesions in fibroblastic cells. Cell Motil. 61, 161–171. https://doi.org/10.1002/cm.20076

Ridley, A.J., 2011. Life at the Leading Edge. Cell 145, 1012–1022. https://doi.org/10.1016/j.cell.2011.06.010

Scarpa, E., Mayor, R., 2016. Collective cell migration in development. J. Cell Biol. 212, 143–155. https://doi.org/10.1083/jcb.201508047

Schindelin, J., Arganda-Carreras, I., Frise, E., Kaynig, V., Longair, M., Pietzsch, T., Preibisch, S., Rueden, C., Saalfeld, S., Schmid, B., Tinevez, J.-Y., White, D.J., Hartenstein, V., Eliceiri, K., Tomancak, P., Cardona, A., 2012. Fiji - an Open Source platform for biological image analysis. Nat. Methods 9, 10.1038/nmeth.2019. https://doi.org/10.1038/nmeth.2019

Schneider, C.A., Rasband, W.S., Eliceiri, K.W., 2012. NIH Image to ImageJ: 25 years of Image Analysis. Nat. Methods 9, 671–675.

Schönichen, A., Geyer, M., 2010. Fifteen formins for an actin filament: A molecular view on the regulation of human formins. Biochim. Biophys. Acta BBA - Mol. Cell Res., Includes Special Section on Formins 1803, 152–163. https://doi.org/10.1016/j.bbamcr.2010.01.014

Schwartz, M.A., 2010. Integrins and extracellular matrix in mechanotransduction. Cold Spring Harb. Perspect. Biol. 2, a005066. https://doi.org/10.1101/cshperspect.a005066

Smilenov, L.B., Mikhailov, A., Pelham, R.J., Marcantonio, E.E., Gundersen, G.G., 1999. Focal Adhesion Motility Revealed in Stationary Fibroblasts. Science 286, 1172–1174. https://doi.org/10.1126/science.286.5442.1172

Stedden, C.G., Menegas, W., Zajac, A.L., Williams, A.M., Cheng, S., Özkan, E., Horne-Badovinac, S., 2019. Planar-Polarized Semaphorin-5c and Plexin A Promote the Collective Migration of Epithelial Cells in Drosophila. Curr. Biol. 29, 908-920.e6. https://doi.org/10.1016/j.cub.2019.01.049

Svitkina, T.M., 2020. Actin Cell Cortex: Structure and Molecular Organization. Trends Cell Biol. 30, 556–565. https://doi.org/10.1016/j.tcb.2020.03.005

Tojkander, S., Gateva, G., Husain, A., Krishnan, R., Lappalainen, P., 2015. Generation of contractile actomyosin bundles depends on mechanosensitive actin filament assembly and disassembly. eLife 4. https://doi.org/10.7554/eLife.06126

Tojkander, S., Gateva, G., Lappalainen, P., 2012. Actin stress fibers - assembly, dynamics and biological roles. J. Cell Sci. 125, 1855–1864. https://doi.org/10.1242/jcs.098087

Tojkander, S., Gateva, G., Schevzov, G., Hotulainen, P., Naumanen, P., Martin, C., Gunning, P.W., Lappalainen, P., 2011. A Molecular Pathway for Myosin II Recruitment to Stress Fibers. Curr. Biol. 21, 539–550. https://doi.org/10.1016/j.cub.2011.03.007

Tokunaga, M., Imamoto, N., Sakata-Sogawa, K., 2008. Highly inclined thin illumination enables clear single-molecule imaging in cells. Nat. Methods 5, 159–161. https://doi.org/10.1038/nmeth1171

Valencia, D.A., Quinlan, M.E., 2021. Formins. Curr. Biol. 31, R517–R522. https://doi.org/10.1016/j.cub.2021.02.047

Vallenius, T., 2013. Actin stress fibre subtypes in mesenchymal-migrating cells. Open Biol. 3, 130001. https://doi.org/10.1098/rsob.130001

Venken, K.J.T., Schulze, K.L., Haelterman, N.A., Pan, H., He, Y., Evans-Holm, M., Carlson, J.W., Levis, R.W., Spradling, A.C., Hoskins, R.A., Bellen, H.J., 2011. MiMIC: a highly versatile transposon insertion resource for engineering Drosophila melanogaster genes. Nat. Methods 8, 737–743. https://doi.org/10.1038/nmeth.1662

Vignaud, T., Copos, C., Leterrier, C., Tseng, Q., Blanchoin, L., Mogilner, A., Théry, M., Kurzawa, L., 2020. Stress fibers are embedded in a contractile cortical network (preprint). Cell Biology. https://doi.org/10.1101/2020.02.11.944579

Walma, D.A.C., Yamada, K.M., 2020. The extracellular matrix in development. Development 147. https://doi.org/10.1242/dev.175596

Wehrle-Haller, B., Imhof, B.A., 2003. Actin, microtubules and focal adhesion dynamics during cell migration. Int. J. Biochem. Cell Biol. 35, 39–50. https://doi.org/10.1016/S1357-2725(02)00071-7

Zamir, E., Katz, M., Posen, Y., Erez, N., Yamada, K.M., Katz, B.Z., Lin, S., Lin, D.C., Bershadsky, A., Kam, Z., Geiger, B., 2000. Dynamics and segregation of cell-matrix adhesions in cultured fibroblasts. Nat. Cell Biol. 2, 191–196. https://doi.org/10.1038/35008607